RESEARCH ARTICLE

An African-Specific Variant of *TP53* Reveals PADI4 as a Regulator of p53-Mediated Tumor Suppression

Alexandra Indeglia[1,2], Jessica C. Leung[1], Sven A. Miller[3], Julia I-Ju Leu[4], James F. Dougherty[1], Nicole L. Clarke[1], Nicole A. Kirven[1], Chunlei Shao[1], Lei Ke[3], Scott Lovell[5], Thibaut Barnoud[1], David Y. Lu[1], Cindy Lin[6], Toshitha Kannan[7], Kevin P. Battaile[8], Tyler Hong Loong Yang[6], Isabela Batista Oliva[1], Daniel T. Claiborne[6], Peter Vogel[9], Lijun Liu[5], Qin Liu[1], Yulia Nefedova[6], Joel Cassel[1], Noam Auslander[1], Andrew V. Kossenkov[7], John Karanicolas[3], and Maureen E. Murphy[1]

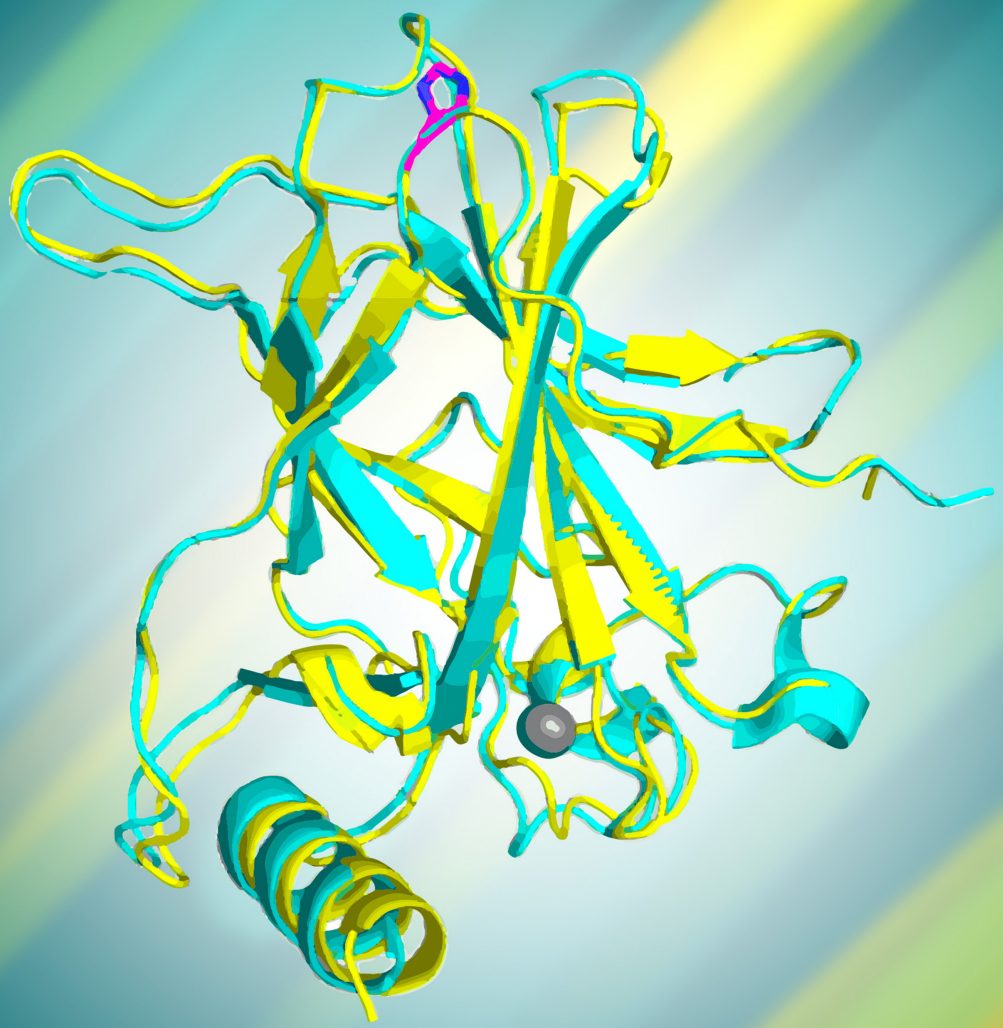

ABSTRACT *TP53* is the most frequently mutated gene in cancer, yet key target genes for p53-mediated tumor suppression remain unidentified. Here, we characterize a rare, African-specific germline variant of *TP53* in the DNA-binding domain Tyr107His (Y107H). Nuclear magnetic resonance and crystal structures reveal that Y107H is structurally similar to wild-type p53. Consistent with this, we find that Y107H can suppress tumor colony formation and is impaired for the transactivation of only a small subset of p53 target genes; this includes the epigenetic modifier *PADI4*, which deiminates arginine to the nonnatural amino acid citrulline. Surprisingly, we show that Y107H mice develop spontaneous cancers and metastases and that Y107H shows impaired tumor suppression in two other models. We show that PADI4 is itself tumor suppressive and that it requires an intact immune system for tumor suppression. We identify a p53–PADI4 gene signature that is predictive of survival and the efficacy of immune-checkpoint inhibitors.

SIGNIFICANCE: We analyze the African-centric Y107H hypomorphic variant and show that it confers increased cancer risk; we use Y107H in order to identify *PADI4* as a key tumor-suppressive p53 target gene that contributes to an immune modulation signature and that is predictive of cancer survival and the success of immunotherapy.

INTRODUCTION

TP53 encodes a critical tumor suppressor, p53, which has numerous roles in protecting cells from oncogenic transformation and stress through the regulation of transcription, metabolism, cell-cycle arrest, apoptosis, senescence, and immune signaling (1–3). The importance of p53 in tumor suppression is evidenced by the fact that this gene is mutated in over half of human cancers. Li–Fraumeni disease is characterized by germline p53 mutations and is associated with an increased risk of multiple primary cancers throughout life (4). Whereas wild-type (WT) p53 is critical for tumor suppression, mutant p53 promotes tumorigenesis through the inactivation of wild-type p53 function, and through the gain of oncogenic properties ("gain of function") caused by new activities of mutant, misfolded p53 protein. Mutant p53 gain of function includes the promotion of proliferation, epithelial-to-mesenchymal transformation, angiogenesis, metastasis, and drug resistance (5–8). In addition to fully inactivating mutations in Li–Fraumeni syndrome, there are over 200 germline variants of *TP53*; some of these, such as G334R and P47S, have been shown to be hypomorphic in function and to be associated with increased cancer risk in humans (9–12).

Although p53 has both cytoplasmic and mitochondrial roles, it is widely accepted that the transcriptional activity of p53 is critical for tumor suppression. Numerous p53 transcriptional targets have been identified for p53 that play roles in apoptosis and growth arrest, such as *BBC3*, *PMAIP1*, and *CDKN1A* (13–15). However, these genes are infrequently mutated in cancer. Moreover, mice deficient in these target genes do not show enhanced rates of spontaneous cancer (16–18). Thus, critical target genes for p53-mediated tumor suppression remain to be identified. In support of this, a recently published CRISPR screen has identified one of the first p53 target genes that itself shows tumor suppressor function: the p53 target *ZMAT3* that regulates RNA splicing (19).

Here, we analyze the germline p53 variant Y107H (Tyr107His, rs368771578), which exists in approximately 0.1% of African-descent individuals (gnomAD v2.1.1) and which we show is hypomorphic in function. We show that, like the other hypomorphic germline variants P47S and G334R, the Y107H variant retains a considerable WT function, is structurally similar to WT p53, and is defective in the transactivation of only a small subset of p53 target genes. The latter subset includes the gene encoding the epigenetic modifying protein PADI4, which deiminates arginine to citrulline and is subject to mutational inactivation in some human tumors (20, 21). Interestingly, *PADI4* shows impaired transactivation by several other p53 hypomorphic variants, suggesting that this p53 target is exquisitely sensitive to p53 function. We show that *PADI4* markedly impairs tumor progression, requires an intact immune system in order to do so, and enhances the ability of p53 to regulate a subset of genes that are predictive of immune cell infiltrates and the efficacy of immune-checkpoint inhibition. Finally, we show that we

[1]Program in Molecular and Cellular Oncogenesis, The Wistar Institute, Philadelphia, Pennsylvania. [2]Graduate Group in Biochemistry and Molecular Biophysics, Perelman School of Medicine, University of Pennsylvania, Philadelphia, Pennsylvania. [3]Program in Molecular Therapeutics, Fox Chase Cancer Center, Philadelphia, Pennsylvania. [4]Department of Genetics, Perelman School of Medicine, University of Pennsylvania, Philadelphia, Pennsylvania. [5]Del Shankel Structural Biology Center, The University of Kansas, Lawrence, Kansas. [6]Program in Immunology, Microenvironment and Metastasis, The Wistar Institute, Philadelphia, Pennsylvania. [7]Program in Gene Expression and Regulation, The Wistar Institute, Philadelphia, Pennsylvania. [8]NYX, New York Structural Biology Center, Upton, New York. [9]Department of Pathology, St. Jude Children's Research Hospital, Memphis, Tennessee.

Corresponding Author: Maureen E. Murphy, Program in Molecular and Cellular Oncogenesis, The Wistar Institute, 3601 Spruce Street, Philadelphia, PA 19104. Phone: 215-495-6870; E-mail: mmurphy@wistar.org

Cancer Discov 2023;13:1–24

doi: 10.1158/2159-8290.CD-22-1315

can identify compounds that exhibit preferential sensitivity in tumors with the Y107H hypomorph. The combined data shed light on cancer disparities in African-descent individuals, personalized medicine approaches, and critical target genes for p53-mediated tumor suppression.

RESULTS

The Y107H Variant Is Comparable with WT p53 for Growth Suppression and Apoptosis

The Y107H variant has previously been reported to be "partially functional" in yeast and mammalian transactivation assays (22, 23). To preliminarily test this assessment, we performed a colony suppression assay in p53-null H1299 cells. This analysis confirmed that Y107H is modestly impaired for colony suppression compared with WT p53, similar to another African-specific p53 hypomorph, P47S (Fig. 1A; Supplementary Fig. S1A for p53 levels). We next compared human lymphoblastoid cells [lymphoblastoid cell lines (LCL)] from age- and ethnicity-matched individuals who harbor WT p53 or are heterozygous for the Y107H variant. Treatment with the DNA-damaging agent doxorubicin led to modestly increased apoptosis in Y107H LCLs as compared with WT p53 and the Li–Fraumeni R273H mutation, as indicated by the increased level of cleaved caspase 3 (CC3) and cleaved lamin A (CLA; Fig. 1B). Similar increased chemosensitivity has been seen for other partially functional mutant p53 alleles (24). In contrast, we found identical sensitivity of these LCLs to other agents, including the ferroptosis-inducing agent RSL3 (Supplementary Fig. S1B).

To further assess the functionality of Y107H, we generated a Y107H knockin mouse using CRISPR-Cas9 editing in C57Bl/6 embryos. This mouse was generated in the background of WT murine p53 (Y104H) or in mice containing the humanized p53 knockin (Hupki) targeting allele (Y107H). Hupki p53 replaces exons 4 to 9 (and intervening introns) of murine p53 with the human sequence, and Hupki p53 has been shown to be fully functional and tumor suppressive in mice (25, 26). Both Y104H and Y107H mice were backcrossed to a C57Bl/6 background for over five generations, and the entire p53 coding region was sequenced to ensure the absence of second-site mutations. Both Y107H and Y104H mouse embryo fibroblasts (MEF) showed similar p53 induction compared with WT p53 (Fig. 1C; Supplementary Fig. S1C and S1D) and again showed modestly increased cell death following doxorubicin treatment compared with WT and p53-null MEFs (Fig. 1C; Supplementary Fig. S1E). Given these differences between WT p53 and Y107H, we clarified that unlike R273H, which shows a significantly reduced ability to transactivate *p21/CDKN1A* in response to nutlin-3a (nutlin), Y107H is indistinguishable from WT p53 in this regard (Supplementary Fig. S1F), further supporting the designation of Y107H as a hypomorph. We next assessed the DNA damage response in Y107H mice following gamma radiation. In the radiosensitive spleen and thymus, Y107H showed increased apoptosis following gamma radiation compared with WT p53, as well as increased Ki-67 staining in the untreated spleen (Fig. 1D and E; Supplementary Fig. S1G and S1H). The increased Ki-67 in Y107H spleen cells, and the moderate increase in apoptosis following doxorubicin and radiation, prompted us to assess the proliferative potential and efficiency of cell-cycle arrest in Y107H LCLs and MEFs compared with WT p53. These analyses revealed significantly increased numbers of cells in the S phase in Y107H LCLs and MEFs compared with WT, as well as decreased growth arrest following treatment with doxorubicin (Supplementary Fig. S1I and S1J). The increased proliferation and decreased ability to undergo growth arrest likely explain the increased apoptosis in Y107H cells following treatment with doxorubicin or gamma radiation, as a correlation between proliferation and increased p53-mediated apoptosis has been noted in previous studies (27, 28).

Y107H Is Defective for Transactivation of a Subset of p53 Target Genes, Including *PADI4*

We next performed RNA sequencing (RNA-seq) on human LCLs with WT p53 or heterozygous for Y107H treated with nutlin or cisplatin. This analysis revealed nearly identical p53 target activation in WT and Y107H LCLs (Fig. 2A and B). Not surprisingly, the p53 pathway was the key pathway differentially regulated (Supplementary Fig. S2A and S2B). Only a small subset of p53 target genes were impaired for transactivation in Y107H LCLs in response to nutlin [$n = 75$, fold change (FC) >2] or cisplatin ($n = 70$, FC >2; Supplementary Fig. S2C; Supplementary Table S1). Among the top impaired p53 target genes in Y107H in response to nutlin was *PADI4*. Analysis of RNA-seq data for LCLs with two other hypomorphs of p53 (P47S and G334R) revealed *PADI4* to be one of only two genes with impaired transactivation in all three hypomorph LCLs compared with matched WT cell lines from age- and ethnicity-matched family members (Supplementary Fig. S2D). We next used qRT-PCR analysis of independent samples in order to confirm that the p53 target *CDKN1A* (p21) shows similar transactivation by WT and Y107H, but that the p53 targets *PLTP*, *PADI4*, and *HHAT* were markedly impaired for transactivation in Y107H cells in response to nutlin (Fig. 2C) and cisplatin (Supplementary Fig. S2E). At the protein level, PADI4 showed impaired upregulation following nutlin treatment in Y107H LCLs; this was also true in LCLs from four other p53 hypomorphs (G334R, P47S, R175C, and Y220H), as well as in LCLs containing the hotspot mutant R273H (Fig. 2D and E). Decreased PADI4 immunostaining was evident in the spleens and thymuses of Y107H mice following gamma radiation (Fig. 2F–H). Because PADI4 is critical for the formation of neutrophil extracellular traps (NET), we analyzed NET formation in phorbol 12-myristate 13-acetate (PMA)–stimulated neutrophils isolated from WT and Y107H mice (29). NETs from Y107H neutrophils were markedly reduced compared with neutrophils from age- and sex-matched WT mice, despite equal numbers of neutrophils in both types of mice (Supplementary Fig. S2F–S2H).

Y107H Is Impaired for Binding at Certain p53 Response Elements

We next performed chromatin immunoprecipitation-quantitative real-time PCR (ChIP-qPCR) for p53 in WT and Y107H LCLs treated with nutlin for 24 hours. ChIP-qPCR analysis revealed the Y107H variant to be modestly impaired for binding to chromatin at its response element for all targets tested, including the canonical p53 targets *MDM2* and

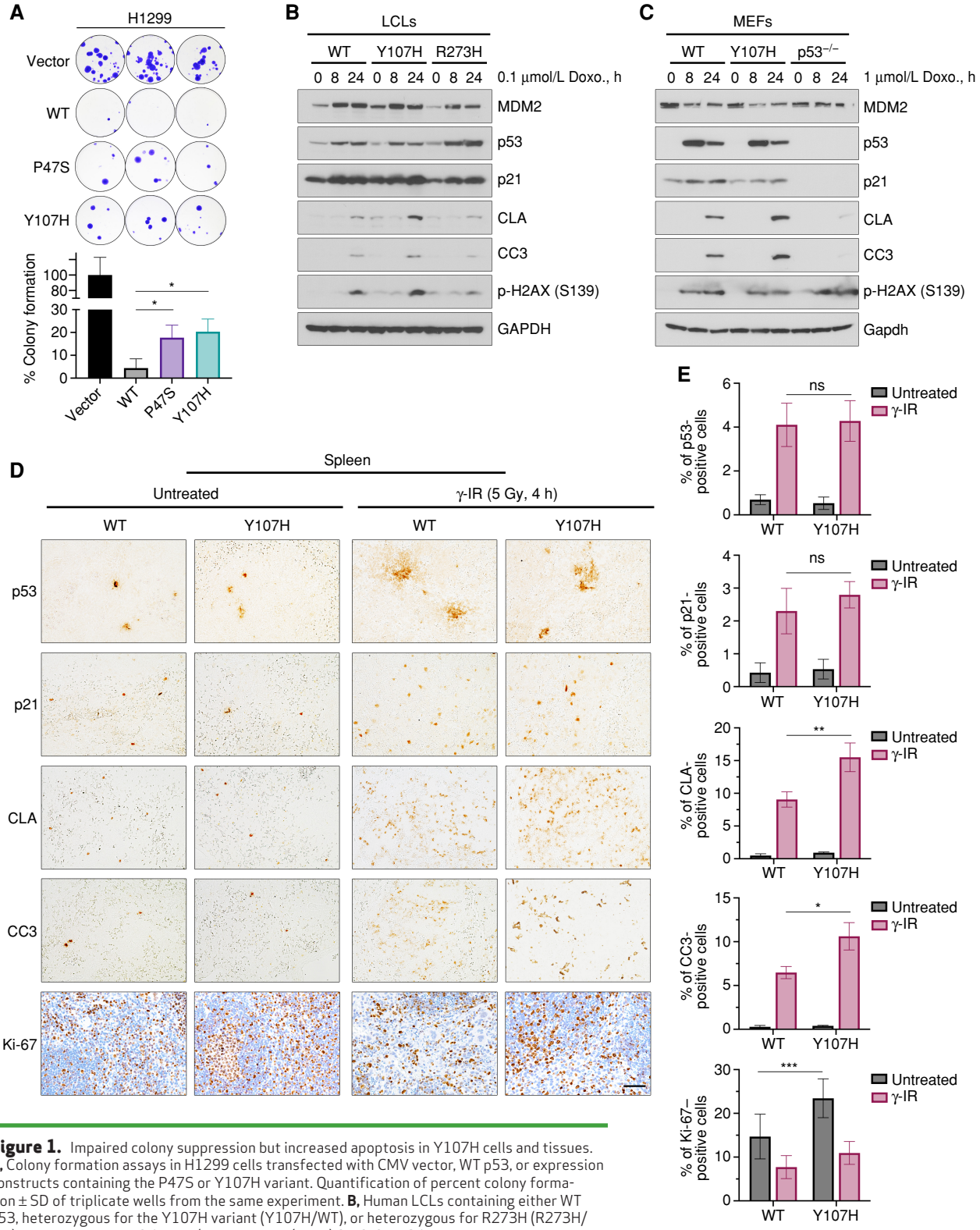

Figure 1. Impaired colony suppression but increased apoptosis in Y107H cells and tissues. **A,** Colony formation assays in H1299 cells transfected with CMV vector, WT p53, or expression constructs containing the P47S or Y107H variant. Quantification of percent colony formation ± SD of triplicate wells from the same experiment. **B,** Human LCLs containing either WT p53, heterozygous for the Y107H variant (Y107H/WT), or heterozygous for R273H (R273H/WT) were treated with 0.1 μmol/L doxorubicin (Doxo) for 0, 8, or 24 hours and assessed by immunoblot for the indicated antibodies. **C,** Homozygous WT, Y107H, or p53$^{-/-}$ MEFs were treated with 1 μmol/L doxorubicin for 0, 8, or 24 hours and assessed by immunoblot for the indicated antibodies. **D,** Representative IHC from Hupki WT mice and Y107H variant mice irradiated with 5 Gy after 4 hours (n = 3 mice per condition) and stained with the indicated antibodies. Scale bar, 50 μm. γ-IR, gamma radiation. **E,** Percentages of positive cells from IHC of WT and Y107H mice in **D**. Averages ± SEM from at least three random images from n = 3 mice per condition. *, $P < 0.05$; **, $P < 0.01$; ***, $P < 0.001$; ns, not significant, two-tailed unpaired t test.

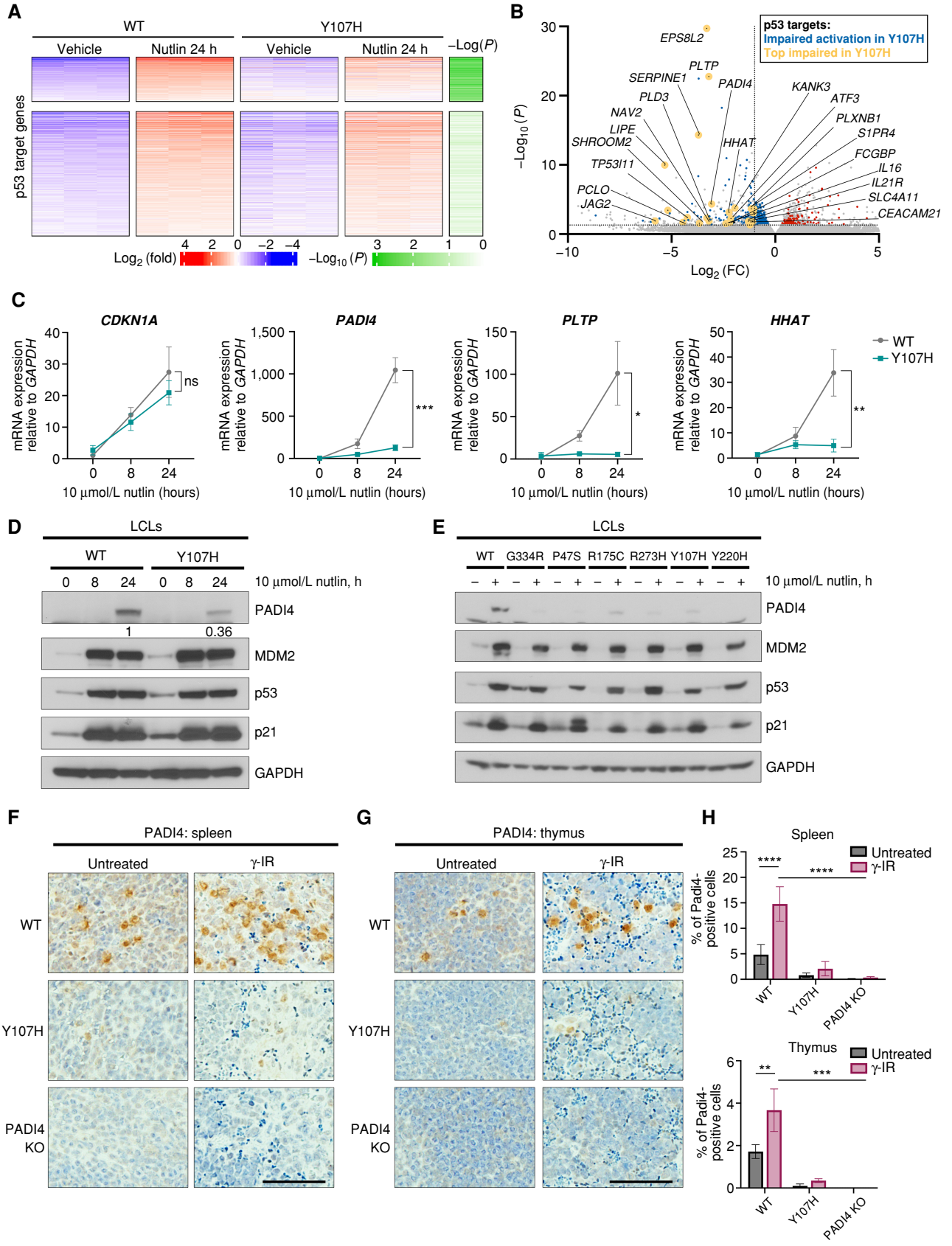

CDKN1A compared with WT p53 (Supplementary Fig. S3A–S3C). Y107H had a more profound impairment for binding to the promoters of *HHAT*, *PLTP*, and *PADI4*, and there was a negligible binding of IgG or with primers for a promoter desert (Supplementary Fig. S3D–S3L). To explore whether this defect in binding was Y107H-intrinsic, we performed direct DNA-binding and fluorescence polarization competition assays using the purified core domains of WT p53 and Y107H (aa 94–312). For these assays, the purified DNA-binding domain was incubated with fluorescently labeled oligonucleotide for the p53 response element from the *CDKN1A* 5′-site (30); unlabeled oligonucleotides representing the p53 response elements for *CDKN1A*, *PLTP,* or *PADI4* were used in increasing concentration as a competitor. Direct binding to the *CDKN1A* response element was markedly impaired in Y107H as compared with WT p53 (Supplementary Fig. S3M and S3N). As expected, WT p53 bound to the response element of *CDKN1A* and *PLTP* in a cooperative manner, as evidenced by a Hill slope >1 (Supplementary Fig. S3O–S3Q). In contrast, Y107H protein showed a defect in cooperative binding to all of the response elements examined (Supplementary Fig. S3O–S3Q). These data suggest that Y107H appears to have an intrinsic defect in DNA binding, but that this defect is less pronounced when assessed *in vivo* by ChIP; this difference may be due to p53, histone, and chromatin modifications that occur *in vivo* that may enhance the ability of Y107H to bind to p53 response elements. Differences in the temperature at which these assays are performed may also have an impact.

Y107H Is Structurally Similar to WT p53 but Shows Increased Propensity to Misfold

The loss of binding at the *PADI4* response element and the apparent loss of cooperativity at multiple sites for Y107H indicate a potential perturbation in p53 structural dynamics. To address this, the purified DNA-binding domain (DBD) of WT and Y107H p53 was analyzed by nuclear magnetic resonance (NMR) spectroscopy (Fig. 3A). We observed modest changes in the Y107H DBD in solution, and all changes were localized to the amino acids directly surrounding Y107H (Fig. 3B and C). Consistent with these data, we found the crystal structure of the core domain of Y107H (aa 94–312) to closely resemble the structure of WT p53 (Fig. 3D and E; Supplementary Fig. S4A–S4C). Despite these modest differences, we found that the core domain of Y107H is thermally destabilized, as indicated by a decrease in melting temperature as measured by differential scanning fluorimetry (DSF; Fig. 3F). Decreased thermal stability is observed in tumor-derived p53 mutants, leading to loss of tumor-suppressive activity and increased propensity to self-aggregate. Using a thioflavin T (ThioT) binding assay to assess protein aggregation over time, we observed that the Y107H core domain showed markedly enhanced aggregation compared with the WT core domain (Fig. 3G). These data prompted us to probe the propensity for Y107H to misfold in cells. Toward this goal, we performed immunofluorescence using antibodies specific for mutant, misfolded p53 (pAb240) or total p53 (CM5). This analysis confirmed a significantly increased propensity for the Y107H variant to misfold into a mutant, pAb240-reactive conformation; this was evident in early-passage MEFs from WT and Y107H mice (Fig. 3H–J; Supplementary Fig. S4D), as well as in oncogenically transformed E1A/Ras MEFs (Supplementary Fig. S4E and S4F). The combined data support the premise that Y107H possesses many WT properties but has an increased propensity to misfold into a mutant conformation.

Y107H Mice Have Increased Rates of Spontaneous and Inducible Cancer

To probe the tumor-suppressive ability of the Y107H variant *in vivo*, we monitored mice harboring either WT p53 or homozygous for the Y107H variant in a C57Bl/6 background for spontaneous tumor formation. Spontaneous tumor formation was rare in WT p53 mice, with only 1 out of 36 mice showing a histiocytic sarcoma after 20 months (Fig. 4A and B). In contrast, over 30% of Y107H mice developed tumors in this time frame; notably, these included tumors commonly associated with Li–Fraumeni syndrome, such as sarcoma, adrenocortical carcinoma, and breast cancer (Fig. 4A–C; Supplementary Fig. S5A–S5E). The average latency of cancer in Y107H mice was 19.5 months; this supports the premise that this variant is a low-penetrance hypomorph and not a fully inactivating mutant, as mice with mutant p53 typically develop tumors between 6 and 12 months. Interestingly, however, we noted several metastatic tumors. We noted increased rates of tumor incidence in mice harboring the mouse variant of p53, Y104H, compared with WT p53 as well (Supplementary Fig. S5B). To further examine the impact of Y107H on cancer incidence, we subjected age- and sex-matched WT and Y107H mice to fractionated radiation and monitored the development of T-cell lymphoma. We saw a nonsignificant increase in T-cell lymphoma in Y107H mice, combined with a significant increase in disseminated disease in these mice (Fig. 4D and E), evident as increased spleen and liver sizes in Y107H mice compared with WT (Fig. 4F–I; Supplementary

Figure 2. The Y107H variant is impaired for transactivation of a subset of p53 target genes, including *PADI4*, *PLTP*, and *HHAT*. **A,** Heat map of significantly upregulated p53 target genes from WT and Y107H LCLs in response to 10 μmol/L nutlin at 24 hours. Top, genes that are less responsive in Y107H. Columns, independent biological replicates ($n = 3$). **B,** Volcano plot of top differentially regulated genes between WT and Y107H LCLs treated with 10 μmol/L nutlin at 24 hours. Genes within the p53 pathway with significantly less response (blue) or more response (red) of at least 2-fold in Y107H vs. WT cells after nutlin treatment are highlighted. Selected p53 targets are highlighted and labeled (yellow). **C,** Quantitative PCR analysis of mean expression ± SD of *CDKN1A* (p21), *PADI4*, *PLTP*, and *HHAT* expression levels in WT and Y107H LCLs after 0, 8, and 24 hours of 10 μmol/L nutlin ($n = 3$ biological replicates). Expression is normalized to *GAPDH*. **D,** Western blot of PADI4 and the p53 target proteins indicated in WT and Y107H cells after 0, 8, and 24 hours of 10 μmol/L nutlin. Densitometry values are included for PADI4 protein levels at 24 hours of nutlin treatment, normalized to GAPDH. Analyses are representative of multiple independent replicates. **E,** Western blot of PADI4 and the p53 target proteins indicated in LCLs with WT p53 and multiple hypomorphic variants of p53. All lines are heterozygous for the hypomorph—that is, hypomorph/WT. R273H is a p53 hotspot mutant. Results are representative of at least 3 independent replicates. **F** and **G,** IHC from Hupki WT, Y107H, and PADI4 knockout (KO) mice irradiated with 5 Gy and analyzed after 4 hours ($n = 3$ mice per condition) and stained for PADI4 expression in the spleen (**F**) and thymus (**G**). Scale bar, 50 μm. **H,** Quantification of percent positive cells from IHC of WT, Y107H, and PADI4 KO mice in (**F** and **G**). γ-IR, gamma radiation. Averages ± SEM from at least three random images from $n = 3$ mice per condition. *, $P < 0.05$; **, $P < 0.01$; ***, $P < 0.001$; ****, $P < 0.0001$; ns, not significant, two-tailed unpaired *t* test.

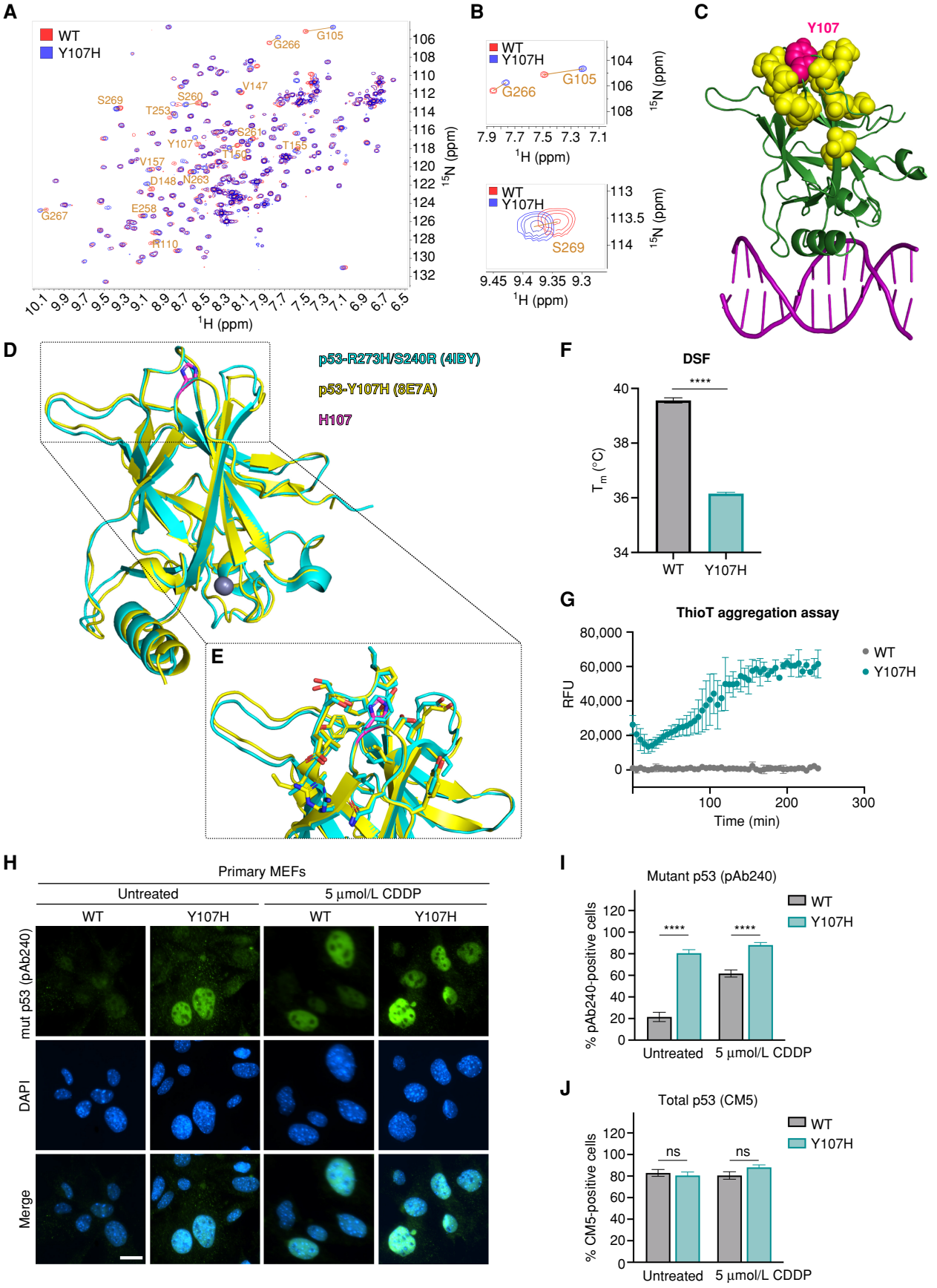

Fig. S5F). Disseminated T-cell lymphoma in these organs was confirmed by $CD3^+/B220^-$ IHC staining (Supplementary Fig. S5G). Interestingly, increased propensity to metastasize is a hallmark of tumors with mutant conformation p53 (31, 32).

WT and Y107H MEFs were transformed with adenovirus E1A and activated (mutant) Ras to further probe the tumor-suppressive ability of the Y107H variant. We confirmed increased Ras and stabilized p53 due to E1A expression by Western blot in two independent sets of WT and Y107H transformed cells (Supplementary Fig. S5H). E1A/Ras MEFs were subcutaneously injected into the flanks of immunocompromised mice, and tumor growth was measured over time. Y107H E1A/Ras tumors grew at a significantly faster rate than WT tumors (Fig. 4J–M). Identical findings were made using an independent set of E1A/Ras-transformed MEFs (Supplementary Fig. S5I–S5K). We noted increased Ki-67 staining in Y107H tumors compared with WT (Supplementary Fig. S5L and S5M). A comparison of the growth of Y107H E1A/Ras tumors to $p53^{-/-}$ E1A/Ras tumors revealed that, as might be expected, Y107H has an intermediate phenotype between p53 null and p53 WT (Supplementary Fig. S5N). The combined data from three different model systems (spontaneous cancer in Y104H and Y107H, as well as E1A/Ras-transformed cells) support the conclusion that Y107H is a significantly poorer tumor suppressor compared with WT p53.

Tumor Cells Containing the Y107H Variant Show Increased Sensitivity to Glutaminase Inhibitors

We previously showed that we could identify chemotherapeutic compounds that show increased sensitivity in tumor cells from another hypomorph, P47S, compared with matched clones with WT p53 (33). To test this premise for Y107H, we used CRISPR/Cas9 to create two independent clones of homozygous Y107H cells in the background of the HCT116 colorectal cancer cell line. These two clones (A11 and C2) of Y107H had the entire p53 cDNA sequenced to confirm the absence of other mutations and were compared with parental HCT116 cells that had gone through the CRISPR knockin process without guides. The Y107H clones exhibited indistinguishable levels of p53 and p53 target activation following treatment with doxorubicin (Supplementary Fig. S6A). We then screened parental HCT116 and both Y107H clones against a 2,000 compound MedChemExpress anticancer library and identified compounds that show preferential loss of viability in both Y107H clones compared with WT (Fig. 5A). In this screen, we identified approximately two dozen compounds that showed a minimum of 3-fold decreased IC_{50} (increased sensitivity) in both Y107H clones compared with parental (Fig. 5B). Two of these compounds were glutaminase inhibitors, CB-839 and BPTES. We confirmed the increased sensitivity of both Y107H clones using an independent cell viability (Alamar Blue) assay (Supplementary Fig. S6B and S6C). We next tested this premise *in vivo*, and NOD scid gamma (NSG) mice were subcutaneously injected with WT or Y107H HCT116 cells and tumor growth was measured. When tumors reached approximately 50 mm^3 in size, mice were assigned randomly to treatment groups and treated with vehicle control or 200 mg/kg CB-839 twice daily by oral gavage. Consistent with our previous findings, vehicle-treated Y107H tumors grew larger than WT tumors (Fig. 5C). Parental HCT116 tumors showed no antitumor effect upon CB-839 treatment, whereas Y107H tumor growth was significantly reduced in the CB-839 treatment group (Fig. 5C–E). There was no loss of weight in treated mice (Supplementary Fig. S6D), and there was no difference in p53 levels in Y107H tumors compared with WT (Supplementary Fig. S6E). Interestingly, the differential sensitivity to CB-839 was not manifested in nontransformed cells, as we saw no evidence for increased CB-839 cytotoxicity in nontransformed Y107H MEFs or LCLs, relative to WT p53, using cell viability assays and clonogenic survival (Supplementary Fig. S6F–S6H). Y107H tumors treated with CB-839 showed significantly decreased Ki-67 and increased markers for programmed cell death (CLA and CC3; Fig. 5F and G). We also noted increased CD31 staining in untreated Y107H tumors (Fig. 5F).

We next probed the ATF4 pathway, which is activated by nutrient deprivation and CB-839 treatment (34). We found evidence for increased induction of ATF4, increased induction of the prodeath protein CHOP, increased CLA, and decreased p-EIF2α in both Y107H clones compared with WT parental cells (Fig. 5H). We recently reported that p53 hypomorphs share common features, including the propensity to misfold (35), so we sought to analyze the P47S hypomorph for CB-839 sensitivity. HCT116 cells with homozygous knockin mutations for the P47S hypomorphs (clones B5 and G12) were generated previously (35). Both P47S clones also showed increased sensitivity to CB-839 and increased induction of CHOP and CLA compared with parental HCT116 cells (Supplementary Fig. S6I and S6J). Interestingly, *PADI4* shows impaired transactivation in both clones of Y107H and P47S compared with parental cells (Supplementary Fig. S6K). Therefore we next sought to determine whether *PADI4* played a role in this differential sensitivity to

Figure 3. Y107H variant shows decreased thermal stability and increased propensity to misfold. **A,** NMR ^1H-^{15}N heteronuclear single quantum coherence spectra of WT (red) and Y107H (blue) core domain. Peaks exhibiting chemical shifts are labeled with the corresponding residue for all with available assignments. **B,** Insets of chemical shifts between WT and Y107H. **C,** Mapping residues with altered chemical shift (yellow) to the protein structure shows that altered residues are spatially grouped near the site of the Y107H mutation (Y107 shown in pink). DNA is included here to indicate the position of the DNA-binding site. **D,** Crystal structure of Y107H. Superposition of $p53^{Y107H}$ [yellow, Protein Data Bank (PDB): 8E7A] with $p53^{R273H/S240R}$ (cyan, PDB: 4IBY). Y107H mutation is shown in magenta. The Zn^{2+} ion is drawn as a gray sphere. **E,** Inset of H107 (magenta) environment in the $p53^{Y107H}$ structure. **F,** The Y107H mutation thermodynamically destabilizes the core domain, as measured via DSF. Mean T_m values ± SEM are shown ($n = 4$ technical replicates). ****, $P < 0.0001$, two-tailed unpaired *t* test. **G,** Aggregation kinetics of the core domain of WT and Y107H at 40°C using ThioT. Aggregation is monitored by relative fluorescence units (RFU) ± SEM to determine ThioT binding ($n = 3$ independent replicates). **H,** WT and Y107H primary MEFs were untreated or treated with 5 μmol/L cisplatin (CDDP) for 24 hours and analyzed by indirect immunofluorescence using mutant p53 conformation-specific antibody (pAb240). Scale bar, 25 μm. **I** and **J,** Quantification of the fraction of cells containing staining for mutant conformation (**I**; pAb240) and total (**J**; CM5) p53. Data are presented as mean ± SD. $n = 25$ random fields of view (>250 cells) from each of 2 independent experiments. ****, $P < 0.0001$; ns, not significant, one-way ANOVA followed by the Tukey multiple comparisons test.

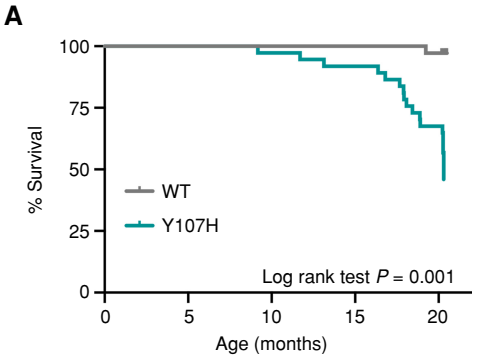

B

Genotype	Tumor type	Age (months)	Gender	Metastasis
WT	HS	19	F	–
Y107H	HCC	20	M	–
Y107H	Osteosarcoma	18	F	+
Y107H	Adrenocortical carcinoma	18	M	–
Y107H	HCC, BCL	20	M	+
Y107H	HS	17	F	+
Y107H	Breast cancer	20	F	–
Y107H	Mesentery tumor	20	F	–
Y107H	Follicular lymphoma	20	F	–
Y107H	HCC	20	M	–
Y107H	BCL	20	M	–
Y107H	Hemangiosarcoma	20	M	–

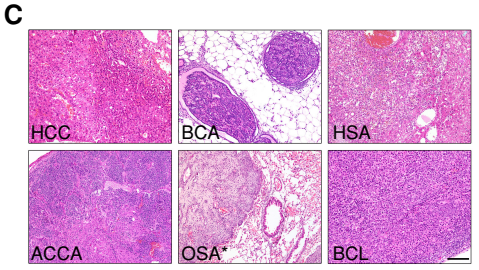

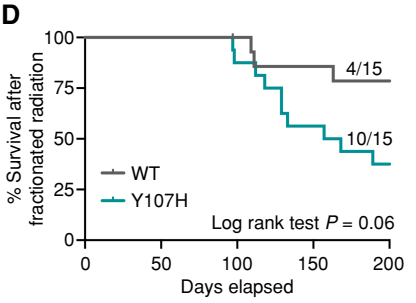

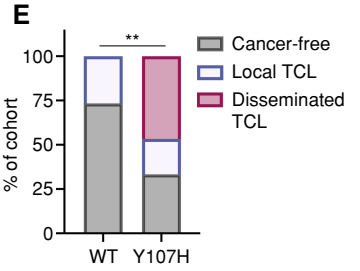

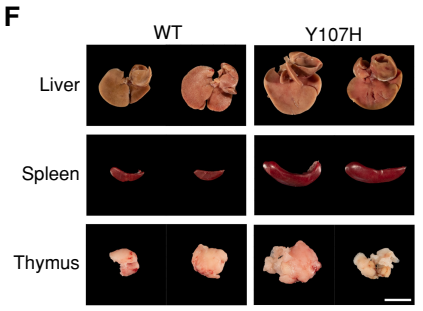

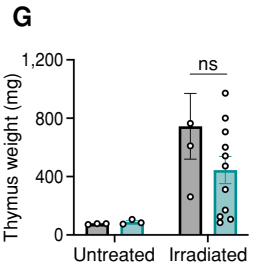

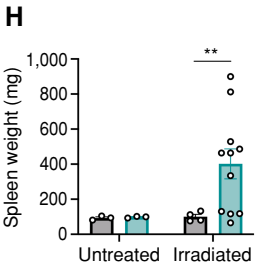

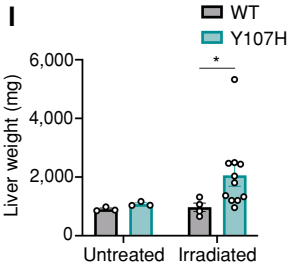

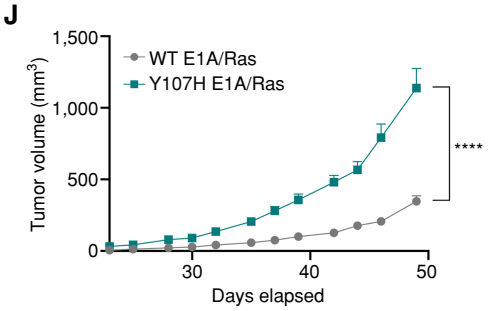

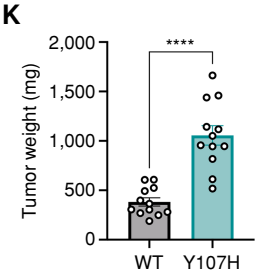

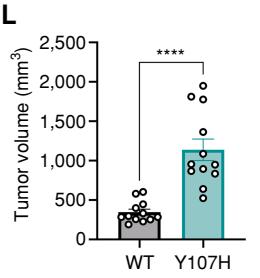

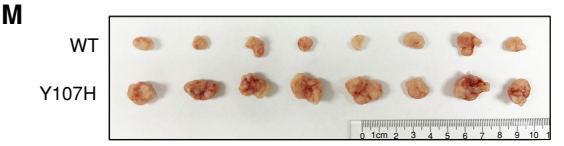

Figure 4. Y107H mice show significantly increased cancer risk. **A,** Kaplan–Meier analysis of survival between Hupki WT p53 ($n = 36$) and Y107H mice ($n = 35$). $P = 0.001$ using a log-rank test. **B,** Summary of cancer incidence in Hupki WT and Y107H mice. Data are representative of 36 WT and 35 Y107H mice. BCL, B-cell lymphoma; HCC, hepatocellular carcinoma; HS, histiocytic sarcoma. **C,** Hematoxylin and eosin staining of tumors from the Y107H mouse. Top left, HCC in the liver. Top middle, breast carcinoma (BCA). Top right, hemangiosarcoma (HSA) within the liver. Bottom left, adrenocortical carcinoma (ACCA). Bottom middle, osteosarcoma (OSA) metastasized to the lung. (The * indicates it is not the primary tumor site but a metastatic lesion in the lung.) Bottom right, BCL in an enlarged lymph node. Scale bar, 100 μm. **D,** Kaplan–Meier analysis of survival between WT ($n = 15$) and Y107H ($n = 15$) mice after fractionated radiation. $P = 0.06$ using the log-rank test. **E,** Proportion of WT and Y107H mice that underwent fractionated radiation with thymic tumors. Analyzed proportion of mice with disseminated lymphoma using Fisher exact test; **, $P = 0.008$. TCL, T-cell lymphoma. **F,** Representative images of liver, spleen, and thymus sizes at the time of harvest in Y107H mice compared with WT following fractionated radiotherapy. Scale bar, 80 mm. **G–I**, Mean weights ± SEM of thymus (**G**), spleen (**H**), and liver (**I**) tissue from healthy age-matched mice or mice that underwent fractionated radiotherapy. **J,** Tumor growth of E1A/Ras-transformed MEFs with WT p53 ($n = 12$) or the Y107H variant ($n = 12$) subcutaneously injected into NOD scid gamma mice. **K–M,** Tumor weights (**K**), tumor volumes (**L**), and representative tumor sizes (**M**) from WT and Y107H E1A/Ras xenografts, shown as mean weights ± SEM. *, $P < 0.05$; **, $P < 0.01$; ****, $P < 0.0001$; ns, not significant, two-tailed paired t test with Welch correction.

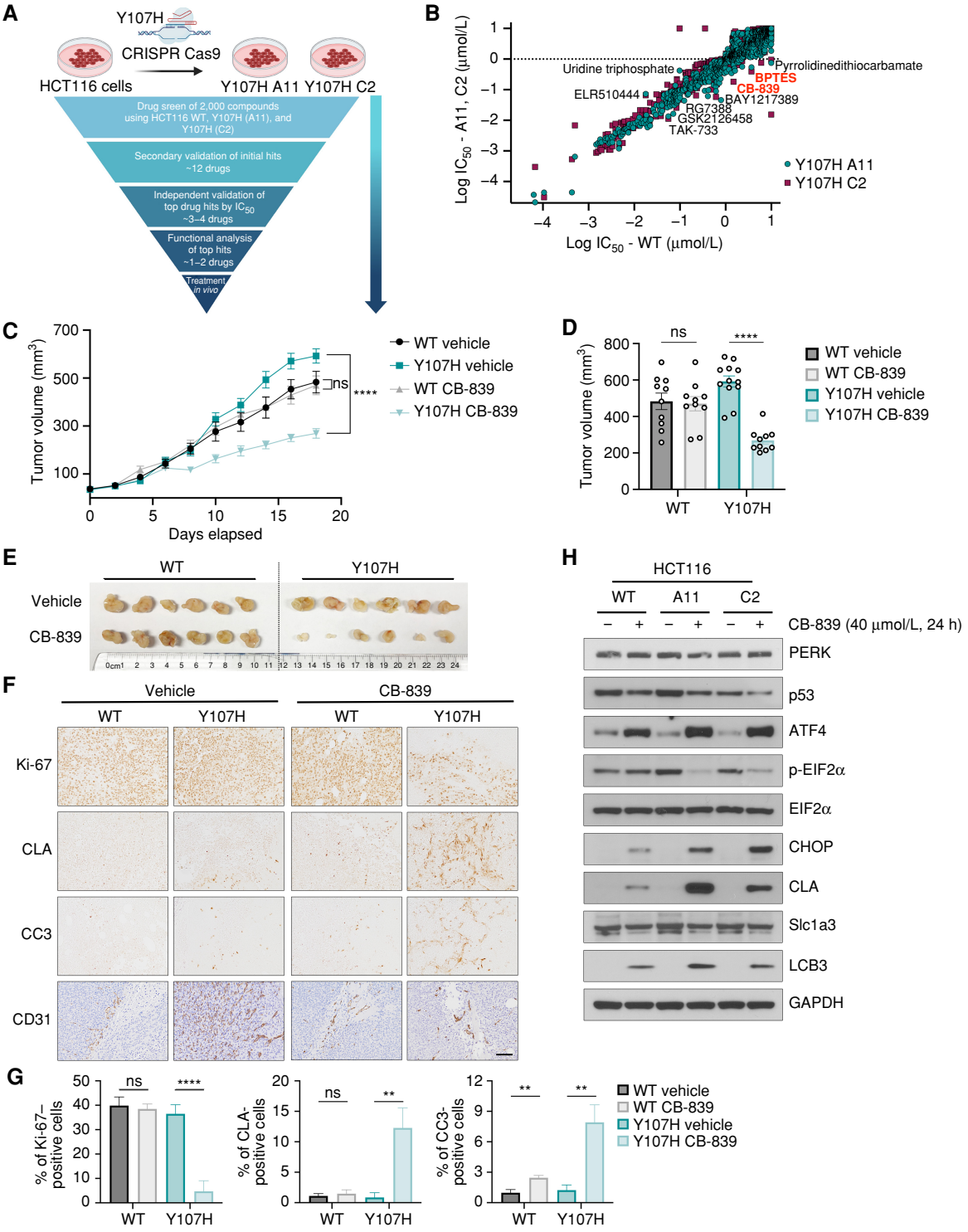

Figure 5. Y107H colorectal cancer cells show increased sensitivity to the glutaminase inhibitor CB-839. **A,** Schematic of CRISPR generation of HCT116 colorectal cancer cells with the Y107H mutation (clones A11 and C2) and subsequent screen for compounds that induce enhanced loss of viability in Y107H clones. (Created with BioRender.com.) **B,** Log IC_{50} of compounds against HCT116 cells with WT p53 or the Y107H clones A11 and C2. Compounds showing significantly increased sensitivity in both Y107H clones are indicated. **C,** Tumor growth of HCT116 cells with WT p53 or Y107H clone A11 in NSG mice ($n = 10$–12 per group) after treatment of vehicle or CB-839. After tumors reached 50 mm^3, vehicle or CB-839 was administered 2× daily by oral gavage. Linear mixed model estimated difference in decreased tumor growth rate (mm^3/day) by treatment with CB-839. ****, $P < 0.0001$; ns, not significant. **D,** Final tumor volume, shown as mean volume ± SEM of HCT116 tumors treated with vehicle or CB-839. ****, $P < 0.0001$; ns, not significant. **E,** Representative images of HCT116 tumors treated with vehicle or CB-839. **F,** Representative IHC from HCT116 tumors ($n = 3$–5 mice per condition) treated with vehicle or CB-839 and stained for the indicated antibodies. Scale bar, 50 μm. **G,** Percentages of positive cells of IHC HCT116 tumors. Averages ± SEM from at least three random images from $n = 3$–5 mice per condition. **H,** HCT116 cells were treated with 40 μmol/L CB-839 for 24 hours and assessed by Western blot for the indicated antibodies. **, $P < 0.01$; ****, $P < 0.0001$; ns, not significant, two-tailed unpaired *t* test with Welch correction.

CB-839. Ectopic expression of *PADI4* in Y107H cells rendered these cells resistant to CB-839 (Supplementary Fig. S6L and S6M). These data support a potential role for *PADI4* in the increased efficacy of glutaminase inhibitors in p53 hypomorph tumors; the underlying mechanism for this effect remains to be elucidated.

PADI4 Interacts with p53, Is Tumor Suppressive, and Cooperates with p53 in the Transcription of a Subset of p53 Target Genes

We next set out to understand the underlying basis for impaired tumor suppression of Y107H, with a particular emphasis on *PADI4*, which we identified as the top impaired p53 target gene in multiple heterozygous p53 hypomorphic LCLs. We confirmed a previous report that *PADI4* is able to suppress colony formation (36) by performing this assay in multiple cancer cell lines, including melanoma (M93-047), lung cancer (A549), bone cancer (U2OS), and colorectal cancer (HCT116; Fig. 6A; Supplementary Fig. S7A–S7E). We also noted significant colony suppression in H1299 lung cells, which are null for p53 (Supplementary Fig. S7D). Analysis of The Cancer Genome Atlas (TCGA) database revealed *PADI4* to be mutated in multiple cancer types, including 8% of melanoma (Supplementary Fig. S7F); indeed, several missense mutations have been shown to impair the enzymatic activity of PADI4 (20). *PADI4* is chiefly expressed in hematopoietic cells, but some tumor cell lines aberrantly express this gene (37). Analysis of over a dozen tumor cell lines containing WT p53 revealed two cell lines with expression of *PADI4*, and this gene was inducible following p53 activation: the M93-047 melanoma (human NRAS-mutant melanoma, WT p53; Supplementary Fig. S7G) and the Yumm1.7 murine melanoma line (BRAF-V600E mutation and PTEN deletion, WT p53; Supplementary Fig. S7H). We next generated clones of Yumm1.7 cells that stably overexpress *PADI4*; interestingly, steady-state levels of p53 protein in this line were increased when PADI4 was overexpressed, and there was increased cell death following etoposide treatment (Fig. 6B). There is evidence that p53 and PADI4 interact (38), so we next probed for a PADI4–p53 interaction in M93-047 cells using a proximity ligation assay; this complex was present in untreated cells, and was greatly induced by nutlin (Fig. 6C). We confirmed a p53–PADI4 interaction using immunoprecipitation–Western blot analysis in Yumm1.7 cells (Fig. 6D). We noted that PADI4 overexpression consistently led to increased p53 steady-state levels; however, this was not due to increased p53 stability, as PADI4 overexpression did not cause an increase in p53 half-life (Supplementary Fig. S7I).

We next sought to dissect the role of PADI4 in tumor suppression. Toward this goal, Yumm1.7 clones stably transfected with vector alone or PADI4 were generated; PADI4 overexpression led to a modest decrease in proliferation in these clones (Supplementary Fig. S7J). These cells were subcutaneously injected into the flanks of C57Bl/6 mice. The PADI4 overexpression clones initially showed faster kinetics of growth compared with vector-alone cells, but tumors rapidly regressed, and by the end of the experiment, 13 of 18 PADI4-overexpressing tumors were not detectable after dissection, resulting in markedly improved survival (Fig. 6E–G; Supplementary Fig. S7K). As an orthogonal approach, we used a CRISPR activation system (CRISPRa) in which deactivated Cas9 (dCas9) activates the expression of the endogenous *PADI4* gene using a PADI4 guide in Yumm1.7 cells; we compared sgControl with PADI4 activation (two independent pools of cells infected with the activation guide) and to a clone in which PADI4 was deleted using CRISPR guides (PADI4 KO). Both independent PADI4 activation clones formed tumors that quickly regressed in C57Bl/6 hosts, whereas PADI4 KO tumors grew significantly larger than sgControl tumors (Fig. 6H). We again saw evidence for an increased p53 steady-state level in PADI4 activation clones relative to KO or sgControl (Supplementary Fig. S7L). RNA-seq analysis revealed a subset of p53 target genes that showed enhanced induction following nutlin treatment in the Yumm1.7 PADI4 activation clones compared with sgControl, supporting the premise that PADI4 may cooperate with p53 to regulate a subset of target genes (Fig. 6I–K). Ingenuity pathway analysis (IPA) revealed roles for this subset of genes in p53, JAK/STAT, IL8, and CXCR4 signaling (Fig. 6J).

We next sought to determine the requirement for p53 in the ability of PADI4 to suppress tumor growth. In addition to the Yumm1.7 clones with CRISPR activation or knockout (KO; Supplementary Fig. S7M), we also created two PADI4 CRISPR activation clones, two PADI4 KO clones, and an sgControl clone in a parental Yumm1.7 cell line that stably expresses a short hairpin for p53 (Yumm1.7 shp53; Supplementary Fig. S7N). We tested these shp53 clones for growth as tumors *in vivo* in syngeneic hosts. We found that PADI4 KO clones still showed increased tumor growth, relative to sgControl, in the absence of p53, suggesting a tumor-suppressive role that is independent of p53. We also found that PADI4 activation was able to suppress tumor growth as well, though perhaps to a reduced extent when p53 is silenced (Supplementary Fig. S7O). These data suggest that PADI4 possesses both p53-dependent and p53-independent tumor suppressor functions.

Increased PADI4 Expression Is Associated with Increased Immune Response and Increased Survival and Response to Immunotherapy in Melanoma Patients

Because enhanced PADI4 expression appeared to activate pathways associated with antitumor immunity, we sought to test the role of the immune system in PADI4-mediated tumor suppression. IPA of Yumm1.7 cells with PADI4 activation (but without nutlin stimulation of p53) revealed activation of immunogenic pathways, including immunogenic cell death pathways, and increased activity of transcriptional regulators such as STAT1 (Supplementary Fig. S8A and S8B). To test the requirement for an immune system in PADI4-mediated tumor suppression, we performed side-by-side experiments in which Yumm1.7 clones (sgControl; KO; and two activation clones, A1 and A2) were monitored as xenografts in mice injected with IgG control or antibody to CD8 to deplete $CD8^+$ T cells. The depletion of $CD8^+$ T cells (Supplementary Fig. S8C and S8D), but not injection with IgG control, completely abolished the ability of PADI4 to suppress tumors in immunocompetent hosts (Fig. 7A). These data support the premise that PADI4 requires an intact immune system in order to suppress tumor development. To follow up on this premise, we found that the ability of PADI4 activation

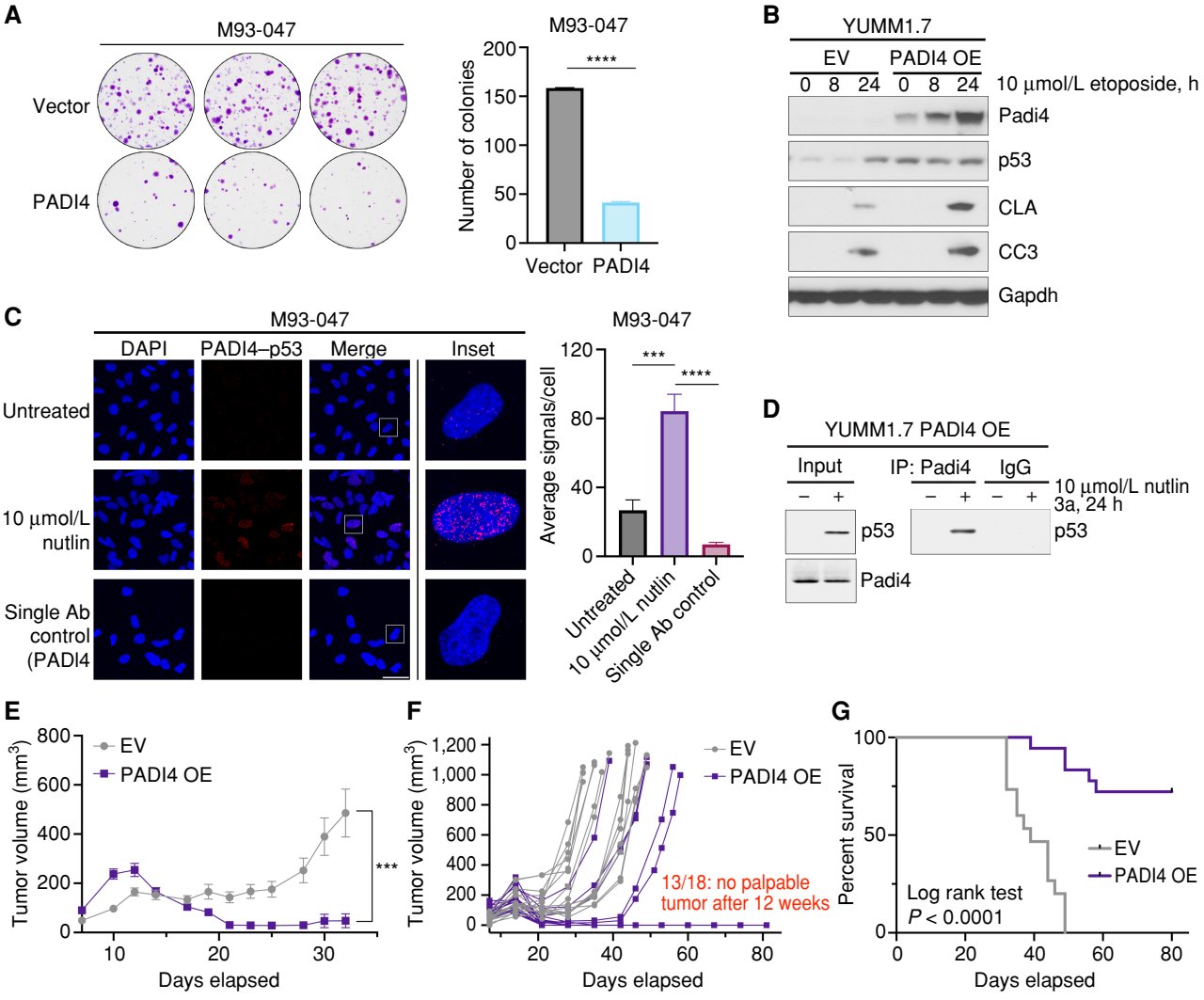

Figure 6. PADI4 interacts with p53 and has tumor-suppressive properties. **A,** Colony formation assays in M93-047 cells transfected with CMV vector alone or expression construct containing WT PADI4. Quantification of mean colony number ± SD of triplicate wells from the same experiment. **B,** YUMM1.7 cells were stably transfected with CMV vector alone or an expression construct containing WT murine PADI4. Cells were treated with 10 μmol/L etoposide for the indicated time points and subjected to Western blot analysis. EV, empty vector; OE, overexpression. **C,** M93-047 cells were treated with 10 μmol/L nutlin for 24 hours, and PADI4–p53 interaction was assessed using a proximity ligation assay. White boxes denote the enlarged insets. Scale bar, 50 μm. Quantification of the average number of proximity ligation assay signals per cell is expressed as mean ± SD. $n = 6$ random fields of view (>100 cells). Ab, antibody. **D,** Immunoprecipitation (IP) of PADI4 from YUMM1.7 cells with stable transfection of murine PADI4 after treatment with vehicle or 10 μmol/L nutlin for 24 hours. Immunoprecipitation of PADI4- or IgG-negative control was followed by immunoblotting for p53. **E–G,** Tumor volumes (**E**), spider plots (**F**), and survival curve (**G**) of YUMM1.7 cells with stable transfection of vector ($n = 16$) or PADI4 ($n = 18$) subcutaneously injected into C57Bl/6 mice. For tumor volumes, data are represented as mean ± SEM. *, $P < 0.05$; ***, $P < 0.001$, two-tailed unpaired t test with Welch correction. Survival curve, $P < 0.0001$ using a log-rank test. (*continued on next page*)

to suppress the growth of Yumm1.7 cells was completely abrogated in immunodeficient NSG mice (Supplementary Fig. S8E–S8G) compared with C57Bl/6 mice (Fig. 7A). To determine whether *PADI4* is correlated with immune responses in human cancers, we first identified p53 target genes that show impaired activation in Y107H cells and that are coexpressed with *PADI4* across multiple TCGA cancer types (Fig. 7B and C). Notably, we found that high expression of these five genes (*PADI4*, *CEACAM21*, *IL16*, *S1PR4*, and *IL21R*) is significantly associated with improved survival in multiple cancer types (Fig. 7D). The average expression of these five genes is also highly associated with increased $CD8^+$ T-cell infiltration in melanoma tumors (Fig. 7E), and they predict improved survival in melanoma following immune-checkpoint inhibitor treatment in two independent datasets (anti–PD-1; Fig. 7F). Because the level of PADI4 expression is associated with WT p53 in multiple cancer types (Supplementary Fig. S8H), these data link tumor suppression by p53 to PADI4 and to a potential immune phenotype.

DISCUSSION

Here, we describe a new African-centric variant of *TP53*, Y107H, which retains the majority of WT p53 function yet

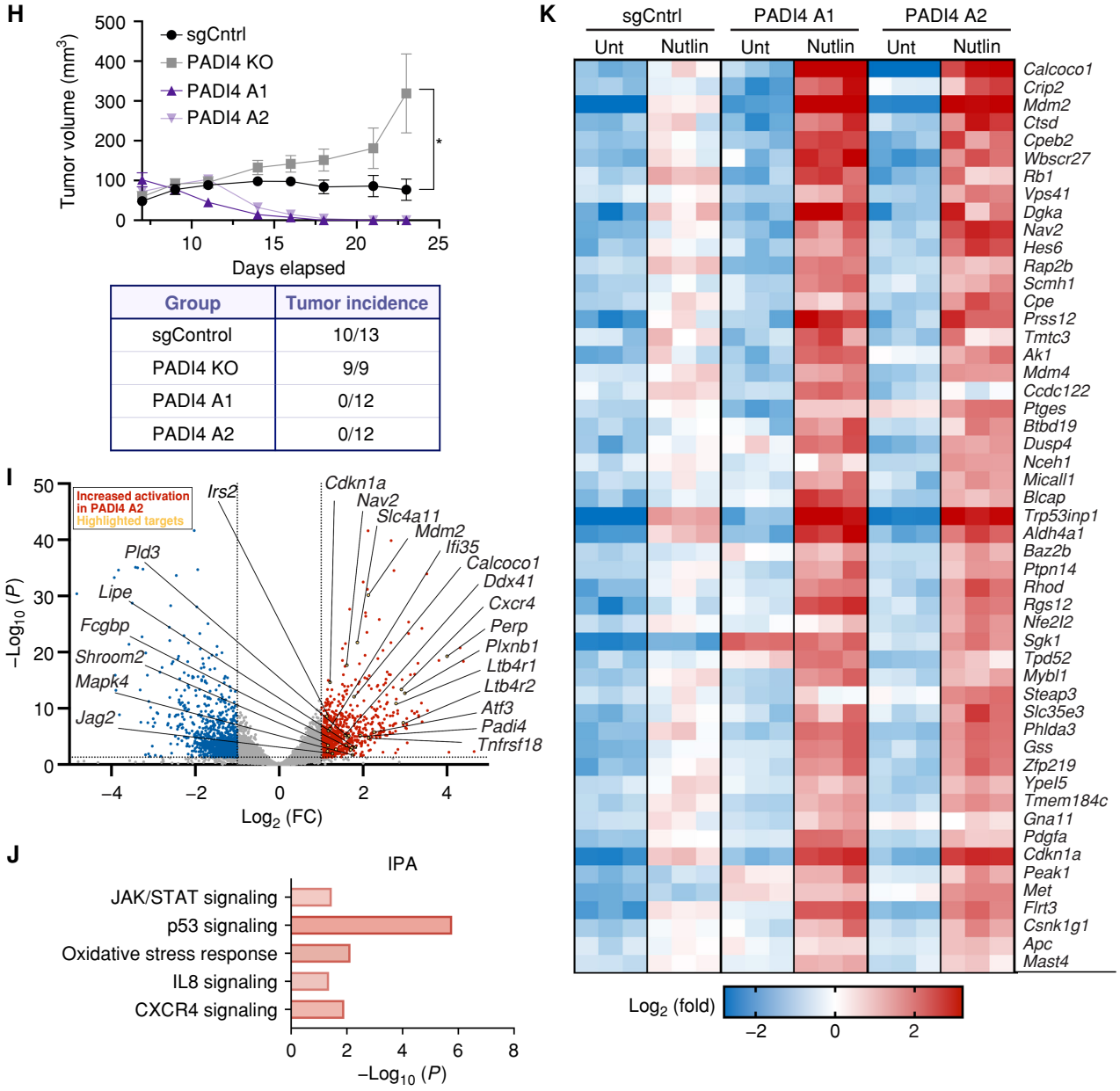

Group	Tumor incidence
sgControl	10/13
PADI4 KO	9/9
PADI4 A1	0/12
PADI4 A2	0/12

Figure 6. ***(Continued)*** **H,** Average tumor volumes of tumor-bearing C57Bl/6 mice subcutaneously injected with YUMM1.7 cells expressing CRISPR machinery for sgControl ($n = 13$), PADI4 KO ($n = 9$), or two independent pools of CRISPRa activation guides for PADI4 ($n = 12$ each). Bottom, tumor incidence for each group is shown in the table. Data, mean ± SEM. **I,** Volcano plot of differentially regulated genes between YUMM1.7 sgControl and PADI4 activation pool 2 treated with 10 μmol/L nutlin for 24 hours. Genes with significantly less responsive (blue) or more responsive (red) of at least 2-fold are highlighted. Selected genes are labeled. **J,** IPA of genes significantly increased in expression in response to nutlin in both PADI4 activation clones compared with sgControl as identified by RNA-seq. **K,** Heat map of top differentially expressed p53 target genes from YUMM1.7 sgControl and both PADI4 activation pools treated with 10 μmol/L nutlin for 24 hours. Columns indicate independent biological replicates ($n = 3$). Unt, untreated.

increases cancer risk in a mouse model. This is consistent with the designation of Y107H as a p53 hypomorph or lesser-functioning allele. Of interest is the fact that colony suppression and transcriptional assays suggest that Y107H retains the majority of p53 function, yet the mice develop cancer; we propose that the Y107H protein may misfold with increasing time, thus explaining the increase in cancer incidence in mice over time. In support of an association between Y107H and cancer risk in humans, it is important to note that this variant was first described in a Li–Fraumeni family (39). Moreover, a comparison of the frequency of Y107H in cancer-affected African Americans in the TCGA database, compared with the frequency of this variant in African Americans in the gnomAD database, is indicative of a positive association of Y107H with cancer ($P = 0.0387$; Supplementary Table S2). Here we used this p53 hypomorph in order to identify key

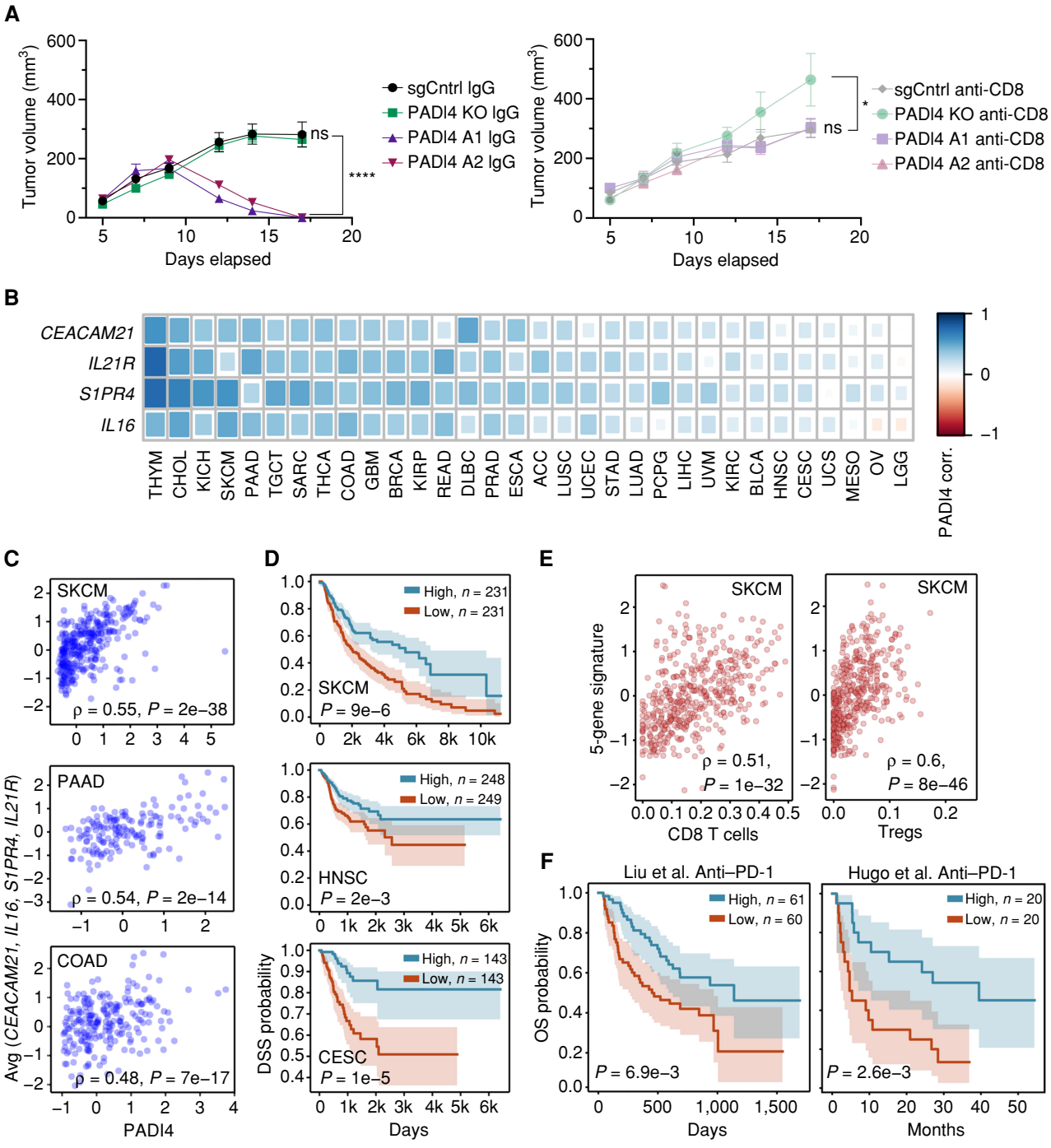

Figure 7. PADI4 suppresses tumor growth in an immune-dependent manner; a PADI4 gene signature predicts survival in cancer and response to anti-PD-1. **A,** Average tumor volumes of tumor-bearing C57Bl/6 mice subcutaneously injected with YUMM1.7 cells expressing CRISPR machinery for sgControl (sgCntrl), PADI4 KO, or two independent pools of CRISPRa activation guides for PADI4. Mice were intraperitoneally injected with IgG (left graph) or anti-CD8 (right graph) prior to tumor injection and once weekly after injection. $n = 10$ mice per condition. *, $P < 0.05$; ****, $P < 0.0001$; ns, not significant, two-tailed unpaired *t* test with Welch correction. **B,** Heat map showing the Spearman rank correlation coefficients correlating the gene expression levels of four genes that are impaired for transactivation by Y107H (*CEACAM21*, *IL16*, *S1PR4*, and *IL21R*) and correlated with *PADI4* expression across TCGA cancer types. **C,** Scatter plots correlating *PADI4* (*x*-axes) with the average (Avg) gene expression level of four genes transactivated by Y107H (*y*-axes) in TCGA skin cutaneous melanoma (SKCM), pancreatic ductal adenocarcinoma (PAAD), and colon adenocarcinoma (COAD). Spearman rank correlation coefficients and *P* values are indicated. DSS, disease-specific survival. **D,** Kaplan–Meier survival curves comparing the survival between patients with a high vs. low (using the median as threshold) 5-gene score (averaging the levels of *PADI4*, *CEACAM21*, *IL16*, *S1PR4*, and *IL21R*) in TCGA SKCM, head and neck squamous cell carcinoma (HNSC), and cervical squamous cell carcinoma (CESC). Log-rank *P* values are indicated. **E,** Scatter plots correlating CIBERSORT-inferred $CD8^+$ T cells and regulatory T cells (Treg; *x*-axes) with the 5-gene score (*y*-axes). Spearman rank correlation coefficients and *P* values are indicated. **F,** Kaplan–Meier survival curves comparing the survival between patients with a high vs. low (using the median as threshold) 5-gene score in two melanoma cohorts of patients treated with anti–PD-1. Log-rank *P* values are indicated. OS, overall survival.

potential target genes through which p53 suppresses tumorigenesis. Transcriptionally, Y107H is able to regulate the majority of canonical p53 target genes, with the exception of a small subset of genes, including *PADI4*. We determined *PADI4* to be one of only two shared p53 targets impaired for transactivation in heterozygous LCLs from three different hypomorphs that are each associated with increased cancer incidence (Y107H, P47S, and G334R). We recently reported that the other p53 target, *PLTP*, also shows tumor-suppressive function (40). Interestingly, *PADI4* transactivation appears to be impaired in several other p53 hypomorphic variants as well, suggesting that this gene may be one of the most sensitive target genes to p53 functional status. We found that this gene is transactivated at somewhat late time points following p53 induction (24 hours), and that both WT and Y107H had quite a low affinity for the *PADI4* p53 response element. Intriguingly, unlike most p53 transcriptional targets, PADI4 expression is restricted largely to hematopoietic cells, with limited expression in the lung and the brain (41), and *de novo* expression in some cancers (42). Additionally, whereas many p53 target genes contain two p53 response elements, typically located in the promoter and first intron, *PADI4* has only a single p53 response element located in the intron (36). These attributes may explain the delayed induction by p53 and/or the sensitivity of this gene to hypomorphic p53 function; this remains to be formally tested.

Although *PADI4* has been identified as a bona fide p53 target gene, there remains a lack of consensus on the role of *PADI4* in cancer. Previous studies have suggested PADI4 to be tumor promoting (43, 44), and it can be found to be overexpressed in some human tumors (37). PADI4 is implicated in the promotion of pluripotency (45, 46) and can positively regulate the transcriptional response by HIF1 (47). Conversely, others have found that PADI4 suppresses tumor colony formation (36), promotes apoptosis (20), inhibits stemness in breast cancer through repression of Nanog and Oct4 (48), and inhibits epithelial-to-mesenchymal transition via citrullination of GSK3β (49, 50). There is a similar lack of consensus on the impact of PADI4 on p53: Whereas one group has shown that PADI4 enhances p53 growth suppression and p53 targets (51, 52), others have shown that PADI4 inhibits the p53-mediated transcription of genes such as *CDKN1A* (38, 53, 54). Here, we show in multiple cancer types that PADI4 can suppress colony formation. We find very low levels of PADI4 in most cancer cell lines tested, contrary to previous reports. Simultaneous observation of tumor growth in both PADI4 KO and PADI4 overexpression clones using the CRISPR activation system revealed that PADI4 clearly has tumor suppressor function. Our data also support the premise that PADI4 overexpression highly activates a subset of p53 target genes associated with immune signaling. However, because PADI4 can citrullinate both histones and other target proteins such as NPM1, GSK3β, and others, it seems likely that the impact of PADI4 on tumor suppression will rely on key target proteins and cell-type specificity. The critical role of PADI4 in the creation of NETs, which can positively affect tumor growth (55), will almost certainly add to the complexity of the role for *PADI4* in tumor suppression. We envision at least two possibilities underlying the immune-mediated tumor-suppressive role of PADI4: The first is that PADI4 is believed to citrullinate some tumor antigens and increase immune recognition; consistent with this, activating SNPs in PADI4 are associated with rheumatoid arthritis (56). The second hypothesis is that p53 and PADI4 cooperate in the transactivation of genes involved in the p53, JAK/STAT, IL8, CXCR4, or innate immune pathways, thus increasing immune recognition of tumors (Fig. 6I–K; ref. 57). These two possibilities are not mutually exclusive. Overall, our data best fit with a model whereby PADI4 possesses both p53-dependent and p53-independent tumor suppressor function, and the majority of PADI4 tumor suppressor function is immune-mediated.

Our group continues to show that we can successfully identify compounds that show enhanced efficacy in tumors with p53 hypomorphs compared with WT p53. We previously showed enhanced cytotoxicity of cisplatin and BRD2/4 inhibitors in E1A/Ras-generated P47S tumors compared with matched WT controls (33, 58, 59). In the present work, we used CRISPR/Cas9 to create two independent homozygous clones of Y107H in the human colorectal line HCT116, and we identified two different glutaminase inhibitors as preferentially cytotoxic in Y107H clones compared with WT. Others have found that p53 regulates the sensitivity to glutaminase inhibitors—in one case through p53-mediated transactivation of *SLC1A3*, an aspartate/glutamate transporter (60), and in another case through transactivation of *SLC7A3*, an arginine importer (61). In our WT and Y107H clones, we failed to see differences in the level of SLC1A3 (Fig. 5H), so we instead analyzed the ATF4/CHOP pathway, and we see evidence for increased ATF4 and CHOP in the Y107H clones, along with increased markers of cell death. Importantly, this increase in cell death in Y107H clones is recapitulated in our Y107H tumors treated with CB-839 (Fig. 5F). We also see increased cell death in two clones of P47S in the HCT116 background (Supplementary Fig. S6I). At present, the role of PADI4 in the sensitivity to glutaminase inhibitors is consistent, but we are unclear as to the mechanism; one possibility that awaits testing is a potential role of amino acid metabolism given the role of PADI4 in arginine/citrulline ratios. In summary, we continue to show that we can provide potentially efficacious treatment options for individuals with germline genetic hypomorphic variants of p53. We also continue to show that genetic differences in the p53 pathway are a possible contributor to cancer disparities in African-descent individuals. And finally, we highlight the premise that understanding the functional defects in biologically relevant hypomorphic variants has the potential to identify key target genes for p53-mediated tumor suppression.

METHODS

Resource Availability

Further information and requests for resources or data should be directed to and will be fulfilled by the corresponding author. The following resources are subject to patent applications and may be shared with research organizations for research only under a material transfer agreement in good faith with the recipient, which may restrict the recipient to make any modifications to this material: constitutive mutant $TP53^{Y107H}$ mouse and HCT116 $TP53^{Y107H}$ cell lines.

Mouse Experiments and Genotyping

All mice were treated in accordance with the regulatory standards of the NIH and American Association of Laboratory Animal Care and were approved by the Wistar Institution of Animal Care and Use Committee (IACUC; Animal Welfare Assurance ID A3432-01). Unless otherwise noted, animal experiments had equal representation of male and female mice. Food and water were provided *ad libitum*. All mice were of C57Bl/6 strain background, apart from NSG mice. NSG mice were acquired from The Wistar Institute Animal Facility. C57Bl/6 WT and PADI4 KO mice were purchased from The Jackson Laboratory. WT Hupki mice were generated as described previously (9). Y107H Hupki mice and Y104H mice were generated by microinjection of Cas9/gRNA ribonucleoprotein complex along with single-stranded oligo deoxyribonucleotide donor (ssODN) into single-cell embryos of WT Hupki mice in the Transgenic Facility at the Fox Chase Cancer Center. For Y107H Hupki mice, the gRNA recognition site is aaaacctaccagggcagctaCGG, with the PAM site in upper case. The ssODN has the following sequence: tgaccgtgcaagtcacagacttggctgtccc agaatgcaagaagcccagacggaaaccgtGGGAgccctggtaggttttctgggaag ggacagaagatgacaggggccaggagggggctggtgc.

For Y104H mice, the gRNA recognition site is aaaacttaccagggcaa ctaCGG, with the PAM site in upper case. The ssODN has the following sequence: 5′-t*c*accgtgcacataacagacttggctgtcccagactgcaggaagcccagg tggaagccatGAttTccctggtaagtttttttgagaagggacaaaagatgacaggggccat ggagtggctgggg*c*a, and each * stands for a phosphorothioate bond. The G is the Y104H mutation (antisense strand), and the two underlined uppercase letters stand for two silent mutations that were introduced to prevent the same gRNA from recutting the Y104H allele. The single-piece synthetic gRNA and ssODN containing two phosphorothioate bonds at each end were ordered from Integrated DNA Technologies and validated in human K562 cells prior to microinjection for efficient introduction of the Y107H mutation. Two independent founders with heterozygous T to C mutations were bred to homozygosity and crossed to C57Bl/6 background for five generations. The entire p53 coding region was amplified and sequenced by the Genomics Facility at The Wistar Institute. Y104H mice were then backcrossed for multiple generations to C57Bl/6 mice.

Cell Culture

For the HCT116 Y107H cell lines, Y107H point mutations were introduced by nucleofection of HCT116 cells with a synthetic gRNA/Cas9 ribonucleoprotein complex along with an ssODN. The gRNA recognition site for Y107H is 5′-aaaacctaccagggcagctaCGG, with the PAM site in upper case, and the ssODN has the following sequence with two phosphorothioate bonds at each end: 5′-tgaccgtgcaagtcaca gacttggctgtcccagaatgcaagaagcccagacggaaaccgtGGGAgccctggtaggtt ttctgggaagggacagaagatgacaggggccaggaggggggctggtgc. Both synthetic gRNAs and ssODNs in ultramer format were purchased from Integrated DNA Technologies. The transfected pools of HCT116 cells were analyzed by using next-generation sequencing for the knockin rate, and single-cell clones were obtained by sorting on a Sony sorter and screened by using next-generation sequencing. Positive clones were expanded, and genotype was confirmed prior to cryopreservation. All clones are negative for *Mycoplasma* contamination and authenticated as HCT116 cells by short tandem repeat profiling. Y107H clones A11 and C2 were confirmed, and the TP53 cDNA was sequenced in its entirety.

Epstein–Barr virus–immortalized human lymphoblastoid cells (LCLs) were acquired from the Coriell Institute (Camden, New Jersey) and cultured in RPMI 1640 (Corning) supplemented with 15% heat-inactivated fetal bovine serum (FBS; HyClone), 1% penicillin/streptomycin (pen/strep; Gibco), and 2 mmol/L L-glutamine (Sigma). WT Hupki and Y107H MEFs, as well as WT (murine p53) Y104H MEFs, were generated as described previously (9). Briefly, embryos were harvested at 13.5 days after development and cultured in DMEM with 1% pen/strep and 10% FBS. E1A/Ras-transformed MEFs and A549 cells were also cultured in DMEM supplemented with 10% FBS and 1% pen/strep. HCT116 and U2OS cells were cultured in McCoy's 5A (Corning) with 10% FBS and 1% pen/strep. H1299 cells were cultured in RPMI 1640 supplemented with 10% FBS and 1% pen/strep. HCT116 $p53^{+/+}$, H1299, U2OS, and A549 were acquired from ATCC. M93-047 cells were a generous gift from Dr. Jessie Villanueva (The Wistar Institute) and were cultured in RPMI 1640 with 5% FBS and 1% pen/strep (62). Yumm1.7 cells were a generous gift from Dr. Marcus Bosenburg (Yale University) and were cultured in DMEM/F12 with 10% FBS, 1% pen/strep, and 1% nonessential amino acids (63). Cells were grown in a 5% CO_2 humidified incubator at 37°C. All cell lines were routinely checked for *Mycoplasma* by the Penn Department of Genetics Cell Culture Services.

Cell Culture Experiments and Treatment

Human lymphoblastoid cells were seeded at 5×10^6 cells per experimental condition, MEFs, Yumm1.7 cells, M93-047 cells, and HCT116 cells were seeded at 1×10^6 to 2×10^6 cells per experimental condition unless otherwise noted. Cells were treated with 10 μmol/L nutlin (Sigma), 5 to 10 μmol/L cisplatin (MedChemExpress), 5 to 10 μmol/L etoposide (SelleckChem), 25 μg/mL cycloheximide (Sigma), 1 μmol/L or 0.1 μmol/L doxorubicin (Cayman), 40 μmol/L CB-839 (SelleckChem), or the appropriate vehicle control for the indicated time points. Cells were harvested at indicated time points and collected by centrifugation at 2,000 rpm for 5 minutes at 4°C, followed by a cold PBS (Corning) wash and additional centrifugation.

Colony Suppression Assays. For colony suppression assays, cells were seeded at 7.5×10^6 to 1×10^6 cells the day before transfection. Cells were transfected with the indicated plasmid using Lipofectamine LTX and Plus Reagent (Invitrogen) for 24 hours. Media were replaced, and cells were allowed to recover for an additional 24 hours, followed by plating 1.0×10^5 to 2.5×10^5 cells (depending on cell type) in triplicate in 6 well plates. Cells were selected in 800 μg/mL G418 (Gibco) for pCMV-Neo-Bam plasmids, pcDNA3.1+ plasmids, and 100 to 400 μg/mL hygromycin (Corning, 50 mg/mL) for pCMV empty vector and pCMV-human-PADI4 (Sino Biologicals) and cultured for 7 to 14 days depending on cell type. A nontransfected control was used for each cell type to observe selection. After observation of colonies, cells were fixed in 10% formalin (Epredia) for 10 minutes and stained with 0.5% crystal violet (Sigma) for 1 hour. Plates were imaged and single colonies were counted using ImageJ.

Clonogenic Survival Assay. For clonogenic survival assays, cells were seeded at 1×10^6 cells the day before treatment. Cells were treated with 100 μmol/L CB-839 for 24 hours. Media were replaced, and cells were plated at a density of 1.0×10^5 and 2.5×10^5 cells in triplicate in 6-well plates. After observation of colonies, cells were fixed in 10% formalin (Epredia) for 10 minutes and stained with 0.5% crystal violet (Sigma) for 1 hour. Plates were imaged, and single colonies were counted using ImageJ.

Generation of Cell Lines. Stable transfection of MEFs was generated as described previously (64). In brief, WT and Y107H cells were seeded at 1×10^6 cells in triplicate the day before transfection. Cells were transfected with pBabe-12S-E1A and pBabe-H-Ras-V12-S35 plasmids donated by Dr. Scott Lowe (Memorial Sloan Kettering Cancer Center) using Lipofectamine LTX and Plus Reagent (Invitrogen) for 24 hours. Media were replaced, and cells were allowed to recover for an additional 24 hours. Cells were then passaged for at least 15 passages to select nonsenescent cells. Cells were sequenced for p53 status and probed for Ras expression and p53 stability to confirm stable transfection. For the stable transfection of YUMM1.7 cells, cells

were seeded at 1×10^5 cells in triplicate the day before transfection. Cells were transfected with pcDNA3.1+ empty vector or pcDNA3.1+ PADI4 (murine) using Lipofectamine LTX and Plus Reagent for 24 hours. Media were replaced, and cells were allowed to recover for an additional 24 hours. Cells were then selected using 800 μg/mL G418 (Gibco) for 10 days. For the generation of *PADI4* CRISPR activation and CRISPR KO cell lines, YUMM1.7 cells or Yumm1.7 shp53 cells were seeded at 1×10^5 cells in triplicate the day before infection. Infection was carried out according to the manufacturer's protocol (Santa Cruz Biotechnology). In brief, cells were infected in 5 μg/mL polybrene and the associated lentiviral activation or KO particles at a multiplicity of infection of 4. Media were replaced, and cells were allowed to recover for an additional 24 hours. Polyclonal lines were selected via puromycin dihydrochloride (sc-108071), hygromycin B (sc-29067), and blasticidin S HCl (sc-495389) for activation lines and puromycin dihydrochloride for PADI4 KO lines. Cells were probed for PADI4 expression via Western blot analysis to confirm stable transfection.

Immunoblot

Whole-cell lysates were made with RIPA buffer [20 mmol/L Tris-HCl (pH 7.5), 150 mmol/L NaCl, 1 mmol/L Na_2EDTA, 1 mmol/L EGTA, 1% NP-40, 1% sodium deoxycholate, 2.5 mmol/L sodium pyrophosphate, 1 mmol/L beta-glycerophosphate, 1 mmol/L Na_3VO_4, 1 μg/mL leupeptin, and complete protease inhibitor mix, Sigma]. After centrifugation, protein concentrations were measured by a BCA protein assay (Bio-Rad). For immunoblotting, 10 to 50 μg of protein lysates were separated by SDS-polyacrylamide gel electrophoresis, transferred onto 0.45-μm PVDF membranes (Millipore), blocked with 5% milk or 5% bovine serum albumin in TBS with 0.1% Tween for 1 hour, and probed with the following antibodies overnight at 4°C: p53 (1C12, Cell Signaling Technology, #2524) for murine p53, p53 (DO-1, Santa Cruz, #sc-126) for human p53, p21 (Cell Signaling Technology, #64016) for murine p21, p21 (12D1, Cell Signaling Technology, #2947) for human p21, MDM2 (IF2/2A10, Millipore, #OP46T and #OP115) for murine MDM2, MDM2 (D1V2Z, Cell Signaling Technology, #86934) for human MDM2, CLA (Cell Signaling Technology, #2035), CC3 (Asp175, Cell Signaling Technology, #9661), phospho-Histone H2A.X (Ser139, Cell Signaling Technology, #2577), PADI4 (Antibodies-online, #ABIN2856939), PERK (C33E10, Cell Signaling Technology, #3192), ATF4 (D4B8, Cell Signaling Technology, #11815), phospho-EIF2α (Ser51, Cell Signaling Technology, #3597), EIF2α (L57A5, Cell Signaling Technology, #2103), CHOP (L63F7, Cell Signaling Technology #2895), Slc1a3 (EAAT1 D20D5, Cell Signaling Technology, #5685), LCB3 (D11, Cell Signaling Technology, #3868), and Ras (C18, BD Biosciences, #610001). Rabbit or mouse IgG secondary antibodies conjugated to horseradish peroxidase were used (Jackson ImmunoResearch), followed by a 5-minute treatment with ECL. Protein levels were detected using autoradiography.

IHC

Tissues were harvested and fixed in 10% formalin overnight at 4°C, followed by a wash with 1× PBS, and then placed in 70% ethanol prior to paraffin embedding. The Wistar Institute Histotechnology Facility performed the tissue embedding and sectioning. Hematoxylin and eosin (H&E) staining and IHC were performed on paraffin-embedded tissues using standard protocols. IHC was performed using antibodies directed against p53, PADI4 (GeneTex, #GTX113945), p21 (EPR10821, Abcam # ab188224), CLA (Cell Signaling Technology, #2035), CC3 (Asp175, Cell Signaling Technology, #9661), Ki-67 (D2H10, Cell Signaling Technology, #9027), CD31 (D8V9E, Cell Signaling Technology, #77699), B220 (RA3-6B2, Thermo, #14-0452-82), and CD3 (Agilent, #A0452). For the IHC studies, paraffin-embedded tissue sections were deparaffinized in xylene and rehydrated in ethanol (100%–95%–85%–75%) followed by distilled water. Samples underwent antigen retrieval by steaming slides in 10 mmol/L citrate buffer (pH 6) or Tris-EDTA buffer (10 mmol/L Tris, 1 mmol/L EDTA, pH 9) for 10 to 15 minutes. Endogenous peroxidase activity was quenched with 3% hydrogen peroxide for 10 minutes, and slides were incubated in blocking buffer (Thermo) for 1 hour. The slides were incubated with primary antibody overnight at 4°C. The next day, the sections were incubated with HRP-conjugated Goat anti-Rabbit secondary antibody (biotinylated; Vector Laboratories) or antibody compatible with the primary antibody used (1:1,000) for 30 minutes and subsequently incubated with VECTASTAIN Elite ABC HRP Kit (Vector Laboratories) according to the manufacturer's instructions. The sections were washed with PBS in between different incubations. Chromogenic staining was performed using the DAB peroxidase kit (Vector Laboratories), and the sections were counterstained using hematoxylin (H-3401, Vector Laboratories). Slides were imaged using a Nikon 80i upright microscope, and at least three random fields were taken per section. Quantification of positively stained cells was done by counting three to five random fields of two sections each per tissue at 10× or 20× magnification using ImageJ software. The percentage of positive nuclei relative to the total number of nuclei was calculated, and differences between samples were analyzed for statistical significance using the Student *t* test.

RNA-seq

Human LCLs were seeded at 5×10^6 cells per condition in triplicate and treated with vehicle control, 10 μmol/L nutlin (Sigma), or 10 μmol/L cisplatin (MedChemExpress) for 0, 8, and 24 hours. RNA was isolated using QIAshredder columns (Qiagen) and the RNeasy Mini Kit (Qiagen) and on-column DNAse digestions. Libraries for 3′ mRNA-seq were generated from 100 ng of DNAseI-treated total RNA using the QuantSeq FWD library preparation kit (Lexogen) according to the manufacturer's directions. Overall library size was determined using the Agilent Tapestation and the DNA 5000 Screentape (Agilent). Libraries were quantitated using real-time PCR (Kapa Biosystems). Libraries were pooled, and high-output, single-end read, 75-base pair next-generation sequencing was done on a NextSeq 500 (Illumina). Reads were aligned using Bowtie2 (65) against mm10 version of the human genome, and RNA-Seq by Expectation Maximization (RSEM; ref. 66) was used to quantify transcripts and estimate fragments per kilobase of transcript per million fragments mapped values using Ensembl transcriptome information. Differentially expressed genes were identified using DESeQ2 (67) both at baseline and for difference in response to treatment. Genes less responsive to treatment in hypomorph than in WT that passed a threshold of FDR <5% were used as inputs for enrichment analysis using Erichr (68) and IPA software (Qiagen, www.qiagen.com/ingenuity) using "Canonical Pathway" and "Upstream Regulator" options.

Quantitative PCR

Cells were lysed using QIAshredder columns (Qiagen), and total RNA was isolated from cell lysates using the RNeasy Mini Kit (Qiagen) and on-column DNase digestions. Then 2 mg total RNA was reverse transcribed using the High-Capacity Reverse Transcription Kit (Applied Biosystems) following the manufacturer's protocol. PCR was performed in triplicate using PowerUp SYBR Green Master Mix and the indicated primer sets (see Supplementary Table S3) under the following conditions: 10 minutes at 95°C, followed by 40 cycles of 95°C for 15 seconds, 60°C for 45 seconds, and 72°C for 1 minute. Quantitative RT-PCR was performed using the QuantStudio 5 Real-Time PCR System (Applied Biosystems). Specificities of PCR products were checked for each primer set and sample via melting curve analysis. Expression levels of genes were normalized relative to levels of GAPDH using the comparative Ct method. Gene expression data are expressed as relative mRNA quantity to vehicle-treated WT controls.

ChIP-qPCR

All reported ChIP-qPCR experiments were performed in 3 independent biological replicates per condition. For each biological replicate, LCLs (2.0×10^7) were treated with vehicle control (DMSO) or 10 μmol/L nutlin (Sigma) for 24 hours and cross-linked with 1% formaldehyde for 10 minutes at room temperature, and subsequently quenched with 0.125 M glycine for 5 minutes. Cross-linked cells were then washed twice in PBS, collected by centrifugation ($2,000 \times g$ for 5 minutes), and lysed in 10 mL swelling buffer [10 mmol/L Tris (pH 7.5), 2 mmol/L $MgCl_2$, 3 mmol/L $CaCl_2$] and placed on ice for 10 minutes. Chromatin fragmentation was performed with a Bioruptor sonication bath (Diagenode, Standard B0101000) at 4°C with the following settings: 25 cycles of high amplitude for 30 seconds, with a 30-second pause in between each sonication. Chromatin was then cleared with centrifugation at maximum speed for 30 minutes at 4°C, 5% saved for input, and immunoprecipitated with antibodies for p53 (DO-1, Santa Cruz), IgG (G3A1, Cell Signaling Technology), and H3K27ac (ab4729, Abcam) overnight at 4°C using magnetic Protein G beads (Dynabeads 10003D, Thermo). Beads were subsequently subjected to two 5-minute washes with ChIP buffer [50 mmol/L HEPES (pH 7.5), 155 mmol/L NaCl, 1.1% Triton X-100, 0.11% Na-deoxycholate, 1 mmol/L EDTA], a 5-minute wash with ChIP buffer with additional 500 nmol/L NaCl, and a 5-minute wash with TE buffer [10 mmol/L Tris-HCl (pH 8.0), 1 mmol/L EDTA]. The cross-link was reversed overnight at 65°C with elution buffer [50 mmol/L Tris-HCl (pH 8.0), 10 mmol/L EDTA, 1% SDS] before treatment with 0.33 mg/mL RNase A (EN0531, Thermo) and 0.5 mg/mL Proteinase K (EO0491, Thermo) at 37°C for 2 hours. DNA was isolated with phenol/chloroform, followed by overnight ethanol precipitation at −20°C. qPCR was used to determine the enrichment of immunoprecipitated DNA relative to the input DNA using gene-specific primer sets to the specified regions (see Supplementary Table S3). Primers directed to a gene desert were used as a negative control.

Fluorescence Polarization Assay

p53 DBD (94-312) constructs (WT and Y107H) were expressed using BL21(DE3) competent cells (Thermo Fisher EC0114) in Terrific Broth (TB) media supplemented with 100 μg/mL (final concentration) ampicillin. Cultures were inoculated with 10 mL overnight culture and grown to OD_{600} 0.5, at which time the temperature was lowered to 15°C. Expression was induced at OD_{600} 0.8–1.0 with 1 mmol/L IPTG and 150 μmol/L $ZnSO_4$ (final concentrations) with shaking for 16 hours. Cells were pelleted at 4,000 rpm and flash-frozen. Cell pellets were resuspended in 200 mL lysis buffer [50 mmol/L NaPi (pH 7.1), 10 mmol/L BME] supplemented with 0.1 mg/mL lysozyme, 0.05 mg/mL DNase I, 10 μmol/L leupeptin, 1 μmol/L pepstatin, 1 mmol/L PMSF, 0.3 μmol/L aprotinin, and 1 mmol/L benzamidine HCl (final concentrations). Lysis was performed using sonication at 40% amplitude for 15 seconds on and 45 seconds off for a total of 15 minutes on. Lysates were clarified via centrifugation at 14,000 rpm for 45 minutes prior to loading onto six tandem 5 mL HiTrap SP HP cation exchange columns (Cytiva 17115201) at 5 mL/minute. The column was washed with Buffer A [50 mmol/L NaPi (pH 7.1), 2 mmol/L BME] and protein eluted using a series of 5% step gradients with Buffer B [50 mmol/L NaPi (pH 7.1), 2 mmol/L BME, 1M NaCl] over 20 CVs at a flow rate of 5 mL/minute. Fractions containing p53 constructs were verified using SDS-PAGE, pooled, concentrated for injection over a HiLoad 16/600 Superdex 75 pg column (Cytiva 28989333), and isocratically eluted in sizing buffer [50 mmol/L NaPi (pH 7.6), 2 mmol/L BME, 5% glycerol, 500 mmol/L NaCl]. Pure fractions were again confirmed using SDS-PAGE and then dialyzed into 50 mmol/L NaPi (pH 7.2), 1 mmol/L TCEP, 10% glycerol, and 150 mmol/L NaCl overnight at 4°C with stirring. Aliquots were then flash-frozen and stored at −80°C. Fluorescently labeled p21–5′-site (5′Alexa Fluor 488-ATGAGGAACATGTCCCAACAT GTTGAGCTC 3′) at 1 μmol/L and unlabeled competitor sequences at 1 mmol/L stocks were reannealed using a thermocycler (95°C for 5 minutes and then decrease at 1°C/minute, hold 20°C). Apparent K_D values were determined by titrating the p53 construct against constant labeled CDKN1A 5′-site DNA (1 nmol/L final concentration) in 50 mmol/L NaPi (pH 7.2), 10% glycerol, and 1 mmol/L TCEP at 25°C for 1 hour before reading. Competition assays were conducted by premixing 2× stocks for p53/p21–5′-site DNA (48 nmol/L for WT and 1.16 μmol/L for Y107H) corresponding to 1.75x apparent K_D in the presence of 2 nmol/L labeled CDKN1A 5′-site DNA and incubated at 25°C for 30 minutes. Competition oligonucleotides were then subjected to serial dilutions at a 2× concentration in 100 μL volume in black opaque flat bottom plates (Greiner Bio-One 655209). Preincubated p53/CDKN1A 5′-site DNA was then combined in a 1:1 ratio with competition oligo dilutions for a final well volume of 200 μL and incubated at 25°C for 1 hour. Data were collected using 458 nm excitation and 528 nm emission filters on a SpectraMax i3x multimode microplate reader (Molecular Devices). All curves were fit using shared parameters for upper and lower baselines for WT and Y107H, respectively (Prism).

Protein Expression, Purification, and NMR Analysis

Protein Expression and Purification. A plasmid was graciously provided by Stewart Loh (Upstate Medical University) for the expression of WT p53 residues 94–312 (the DBD; pET-23^+ vector, no tags on p53). A Y107H missense mutation was introduced via site-directed mutagenesis. The plasmid (mutant or WT) was freshly transformed into *Escherichia coli* BL21 (DE3) competent cells (NEB), and a single colony was used to inoculate an overnight starter culture in TB media. This culture was then used to inoculate the main culture at a 1:100 dilution. The main culture was grown at 37°C shaking at 200 rpm to reach an OD of 0.6 to 0.8, cooled to 25°C, and then induced with 1 mmol/L isopropyl β-d-1-thiogalactopyranoside (IPTG) for 18 to 20 hours at 15°C. Cells were then spun down by centrifugation at $3,500 \times g$ for 20 minutes, and the pellet was resuspended in lysis buffer [50 mmol/L NaPi, (pH 7.7), 10 mmol/L DTT, and 1 mmol/L benzamidine hydrochloride hydrate] and then passed through an Avestin EmulsiFlex-C3 high-pressure homogenizer for 5 rounds. The cell lysate was further spun down at $19,000 \times g$ for 30 minutes, and then the supernatant was collected and filtered through a 0.22-μm PES syringe filter. The filtered supernatant was then purified on an ÄKTA Pure 25—first with HiTrap SP HP cation exchange column and then with a HiTrap Heparin HP affinity column (Cytiva). In both cases, the protein was eluted with 1 M NaCl. The selected fractions were concentrated to at least 1 mg/mL and exchanged with 50 mmol/L NaPi (pH 6.3) and 1 mmol/L DTT.

NMR Analysis. ^{15}N-labeled protein was grown in a starter culture and used to inoculate 500 mL of TB broth, which was grown overnight. This culture was then centrifuged, and the pellet was resuspended in 1 L of M9 media. This was allowed to grow to 1.7 OD and then induced with 1 mmol/L of IPTG. Cells were then harvested and purified using the same method as described above. The protein was concentrated to 200 μmol/L in 25 mmol/L NaPi (pH 7.1) 150 mmol/L KCl, and 5 mmol/L DTT buffer, and 20 μL of D_2O was added to 300 μL of protein for each sample. Spectra were collected on a Bruker Ascend 600-Mhz spectrophotometer at 293.1K. Data were processed using TopSpin 4.0 and MestReNova 12.

Crystallization and Data Collection

Purified p53-Y107H was concentrated to 10.6 mg/mL (0.43 mmol/L) in 150 mmol/L NaCl, 50 mmol/L Na phosphate (pH 7.2), and 1 mmol/L TCEP. A 25 mmol/L stock solution of inhibitor SM0.2

was prepared in DMSO, added to a concentration of 1 mmol/L to an aliquot of the protein, and incubated on ice for approximately 1 hour. A DNA sample (DNA-P21-mouse) was annealed and added to a concentration of 0.11 mmol/L (1:4 DNA:protein) and incubated for 1 hour prior to screening. All crystallization experiments were set up using an NT8 drop-setting robot (Formulatrix Inc.) and UVXPO MRC (Molecular Dimensions) sitting-drop vapor diffusion plates at 18°C. Protein (100 nL) and 100 nL of crystallization solution were dispensed and equilibrated against 50 μL of the latter. Crystals displaying a needle morphology were observed within approximately 1 week from the Index HT Screen (Hampton Research) condition H11 [30% (w/v) PEG 2000 MME, 100 mmol/L potassium thiocyanate]. A cryoprotectant composed of 80% crystallant and 20% glycerol was layered onto the drop, and samples were harvested and stored in liquid nitrogen for X-ray diffraction data collection.

Structure Solution and Refinement. X-ray diffraction data were collected at the National Synchrotron Light Source II (NSLS-II) beamline 19-ID (NYX) using a Dectris Eiger2 XE 9M pixel array detector. Intensities were integrated using XDS (69, 70) via autoPROC (71), and the Laue class analysis and data scaling were performed with Aimless (72). Structure solution was conducted by molecular replacement with Phaser (73) using a search model from a previously determined p53 structure [Protein Data Bank (PDB): 1TSR]. The top solution was obtained in the space group $P2_12_12$ with one molecule in the asymmetric unit. Refinement and manual model building were conducted with Phenix (74) and Coot (75), respectively. Disordered side chains were truncated to the point for which electron density could be observed at a 1.00 sigma level. Structure validation was conducted with MolProbity (76), and figures were prepared using the CCP4MG package (77). Superposition of structures was conducted using GESAMT (78) via the CCP4 (79) interface. Relevant crystallographic data are provided in Supplementary Table S4.

Analysis. The structure of p53-Y107H contains two molecules in the asymmetric unit and adopts a fold typically observed for p53 constructs. Although the protein was crystallized in the presence of inhibitor SM26.1 and DNA, no electron density consistent with this compound or DNA was observed. A search of the PDB revealed one p53 structure with similar unit cell parameters (PDB 4IBY), which is that of a double mutant form R273H/S240R. Superposition of the subunit A chains yielded a root mean square deviation of 0.77 Å between Cα atoms for 196 residues aligned (Supplementary Fig. S4A). Residues that coordinate the Zn^{2+} ions as well as the location of H107 are shown in Supplementary Fig. S4B.

DSF

DSF was carried out using 8 μmol/L protein and 10× SYPRO Orange (Invitrogen) in an assay buffer of 50 mmol/L NaPi (pH 6.3), 100 mmol/L NaCl, and 1 mmol/L DTT. Samples were heated at a rate of 1°C/second from 25°C to 65°C in an Eppendorf Realplex2 Mastercycler and monitored using the JOE emission filter (550 nm). Samples were run in 4 replicates on 2 separate days. The protein's apparent melting temperature was determined from each curve as the midpoint between the highest and lowest fluorescence values in the unfolding curve.

ThioT Binding Assay

ThioT was dissolved in assay buffer [50 mmol/L NaPi (pH 7.2), 5% glycerol, 1 mmol/L TCEP] and centrifuged at 13,000 rpm for 10 minutes to remove particulates prior to concentration determination using an extinction coefficient of 36/(mmol/L)/cm at 412 nm. p53 DBD constructs and ThioT were combined in black, clear bottom plates (Thermo, #265301) at final concentrations 50 and 30 μmol/L, respectively, and then covered with adhesive plate seals (Fisher 08-408-240). Aggregation was monitored using a SpectraMax i3x multimode microplate reader (Molecular Devices) at 40°C for over a 4-hour period with 3 seconds of shaking prior to every read (5-minute intervals), using an excitation filter of 450 nm and emission filter of 490 nm. Data were plotted using Prism.

Immunofluorescence and Proximity Ligation Assay

Cells were grown on Lab-Tek II 8-well chamber slides and were either untreated or treated with 5 μmol/L cisplatin for 24 hours. Cells were fixed in 4% paraformaldehyde (Electron Microscopy Sciences) for exactly 10 minutes, followed by 3 washes in 1× PBS and permeabilization with 0.25% Triton X-100 (Millipore Sigma) for 5 minutes. For immunofluorescence staining, cells were washed 3× with 1× PBS, and blocked for 1 hour at room temperature in a blocking buffer consisting of 4% normal goat serum (Jackson ImmunoResearch) and 1% bovine serum albumin (Sigma-Aldrich) in PBS. Cells were incubated overnight at 4°C with the following primary antibodies diluted in blocking buffer: anti-p53 (CM5, Leica) and anti-p53 (mutant; pAb240, Santa Cruz Biotechnology). Cells were washed 3× with 1× PBS and incubated with the following secondary antibodies at room temperature for 1 hour: Alexa Fluor 488 AffiniPure Goat anti-Mouse IgG (Jackson ImmunoResearch) and Alexa Fluor 594 AffiniPure Goat anti-Rabbit IgG (Jackson ImmunoResearch). Cells were mounted with media containing DAPI, and images were captured using a Nikon TiE automated inverted microscope. Protein–protein interactions were assessed using the PLA Duolink *in situ* starter kit (Sigma-Aldrich) following the manufacturer's protocol. Images were captured using a Leica TSC SP5 confocal microscope. For immunofluorescence staining, cells were treated with 10 μmol/L Edu (Thermo) 8 hours prior to fixation. Edu incorporation was assessed using the Click-iT EdU Cell Proliferation Kit for Imaging with Alexa Fluor 488 dye (Thermo) following the manufacturer's protocol. Images were captured using a Nikon TiE automated inverted microscope.

Immunoprecipitation

Cell nuclei were harvested by resuspension of the cell pellet in Hypotonic Lysis Buffer [10 mmol/L HEPES (pH 7.9), 1.5 mmol/L $MgCl_2$, 10 mmol/L KCl] with protease inhibitors. Cells were incubated on ice for 15 minutes to allow cells to swell. Following this, 0.5% IGEPAL CA-630 was added and cells were centrifuged to remove the cytoplasmic fraction. Nuclei were resuspended in Immunoprecipitation Buffer [10 mmol/L HEPES (pH 7.9), 100 mmol/L KCl, 0.5% IGEPAL CA-630] with protease inhibitors and homogenized using a TissueLyser (Qiagen). Nuclei were incubated on ice for 15 minutes and pelleted, and protein was quantified. For immunoprecipitation experiments, 0.5 to 3 mg of nuclear protein was added to a final volume of 500 μL with diluted antibody for PADI4 (ProteinTech, 17373-1-AP) or IgG control (Cell Signaling Technology, 2729) and rocked overnight at 4°C. The PADI4 immunocomplexes were captured using Recombinant Protein G (rProtein G) Agarose (Thermo Fisher Scientific) for 1 hour at 4°C. The resins were washed 3 times using the Immunoprecipitation Buffer. PADI4-associated proteins were size-fractionated on Novex 4–20% Tris-Glycine Mini Protein Gels (Thermo Fisher Scientific) and incubated with the p53 antibody (1C12; Cell Signaling Technology) overnight at 4°C. Membranes were incubated with Peroxidase AffiniPure Fragment Donkey Anti-Mouse IgG (H + L; Jackson ImmunoResearch) at 1:10,000 dilution, followed by detection using ECL Western Blotting Detection Reagents (Cytiva RPN2106; Millipore Sigma).

Cell-Cycle Analysis by Flow Cytometry

Human LCLs were seeded at a density of 5×10^6 cells per condition in triplicate and harvested by centrifugation at 1,000 rpm for 5 minutes and washed with PBS. Cells were fixed using 1 mL 70% ethanol while vortexing and incubated for 30 minutes on ice. Cells were washed twice using PBS, transferred to a 12 × 15 mm flow tube, and stained with FxCycle Violet stain (Thermo) and 6 μg/mL RNAse for 30 minutes protected from light. Flow cytometry was performed on LSR14-II color and analyzed using FlowJo software (v.10.8).

Spontaneous Cancer Study

WT and homozygous Y107H mice were housed in the same holding room throughout the duration of the experiment. Mice were observed daily for general health and signs of distress, and weekly for obvious tumor formation. Upon visualization of apparent tumor (i.e., breast lump) or signs of distress, mice were euthanized according to IACUC protocols and tissues suspected to have malignancies were fixed in 10% formalin. When mice reached 20 months of age, all remaining mice were euthanized and checked for signs of tumor formation. At least 3 different levels of each tissue were H&E stained and diagnosed by a board-certified pathologist for the presence and subtype of neoplasia.

Fractionated Radiotherapy and Gamma Irradiation

To induce thymic lymphoma, 4- to 5-week-old WT and homozygous Y107H mice were irradiated at 1.5 Gy weekly for 4 weeks. Mice were observed daily for general health and signs of distress for up to 9 months after the final irradiation date. Mice suspected of thymic lymphoma were euthanized according to IACUC protocols and thymus, spleen, and liver were weighed and fixed in 10% formalin. Representative tissues from each mouse strain were reviewed and diagnosed by a board-certified pathologist using three H&E-stained sections of each tissue. For gamma radiation studies, WT Hupki, Y107H Hupki, WT mouse, Y104H mouse, and PADI4 KO mice ages 4 to 6 weeks were irradiated with 5 Gy and euthanized following 4 hours of radiation. Mice with WT p53 (murine) were used as controls for Y104H mice and PADI4 KO mice.

Xenograft Assays

E1A/Ras $p53^{WT}$ and E1A/Ras $p53^{Y107H}$ were subcutaneously injected into the flanks of 8- to 10-week-old NSG mice at a concentration of 1×10^6 cells in 200 μL PBS. YUMM1.7-engineered cells were subcutaneously injected into the flanks of 8- to 10-week-old C57Bl/6 mice (The Jackson Laboratory) at a concentration of 2×10^6 cells in 200 μL PBS. Once they reached ~50 mm^3, they were measured 3 times a week using a caliper. Tumor volumes were calculated using the following formula: $(L \times W \times W) \times 0.52$, in which L represents the large diameter of the tumor and W represents the small diameter. When the tumor area reached ~1- to 1.5-cm diameter in any mouse, mice were sacrificed and isolated tumors were weighed. Unless otherwise specified, average tumor volume is depicted up until the time of the first sacrifice.

CB-839 In Vivo *Treatment*

HCT116 $p53^{WT}$ and $p53^{Y107H}$ (clone A11) cells were subcutaneously injected into the flanks of 8- to 10-week-old female NSG mice at a concentration of 1×10^6 cells in 200 μL PBS. Once tumors reached ~50 mm^3, mice were separated into groups of similar mouse weight and tumor size. Mice were treated with vehicle or 200 mg/kg CB-839 orally twice a day for 18 days. The vehicle consisted of 25% (w/v) hydroxypropyl-b-cyclodextrin (Roquette) in 10 mmol/L citrate, pH 2. CB-839 was formulated as a solution at 20 mg/mL (w/v) in vehicle; the dose volume for all groups was 10 mL/kg. Tumor volumes and body weights were measured every other day.

CD8 Depletion and Tumor-Infiltrating Lymphocyte Isolation

For CD8 depletion studies, anti-mouse CD8β (Lyt 3.2, clone 53-5.8) and isotype control (rat IgG1; clone HRPN) were administered (5 mg/kg) on the day before implantation, the day after implantation, and weekly thereafter (80). Tumors were harvested from sacrificed mice on day 16 after tumor inoculation. Tumor dissociation was carried out using the Tumor Dissociation Kit and gentleMACS Dissociator (Miltenyi Biotec) according to the manufacturer's instructions. Spleens were dissociated using a 70-μm strainer and washed with PBS. Red blood cells were removed from spleens using RBC lysis buffer (BioLegend) for 10 minutes at room temperature. Tumors and spleens were pelleted and resuspended in R10 media (RPMI 1640, 10% FBS, 1% pen/strep, 1% glutamax, and 1% HEPES) and counted. Cells were resuspended in FACS buffer and blocked in TruStain FcX PLUS (BioLegend) and True-Stain Monocyte Blocker (BioLegend) for 10 minutes, washed, and incubated with the following antibodies for 20 minutes at room temperature prior to analysis: CD45 (30-F11), CD4 (RM4-5), CD8 (53.6-7 and 53.5-8), CD11b (M1/70), NK1.1 (PK136; BioLegend), and CD3 (17A2; BD Biosciences). Samples were acquired on a BD FACS Symphony flow cytometer. Data were analyzed using FlowJo v10 (Treestar Inc.).

Compound Screen

Cells were seeded at 1,000 cells/well in white, tissue culture–treated 384-well plates in 50 μL of complete media using the MicroFlo bulk reagent dispenser (Biotek). The next day, 50 nL of test compounds in 100% DMSO were added using the Janus MDT Nanohead dispenser (PerkinElmer) such that the final DMSO concentration in the assay was 0.1%. The compounds were tested at four concentrations (10 μmol/L, 1 μmol/L, 0.1 μmol/L, and 0.01 μmol/L) and incubated with the cells for 72 hours at 37°C and 5% CO_2. After incubation, 25 μL of CellTiter-Glo reagent was added to the plates using the MicroFlo bulk reagent dispenser and the luminescence was measured on the Envision plate reader (PerkinElmer). Luminescence values were converted to % toxicity where 0% is equal to the luminescence in the absence of test compound (DMSO only) and 100% is equal to the luminescence values from cells treated with 1 μmol/L bortezomib. Estimated IC_{50} values were obtained from nonlinear regression fits of the % toxicity values at the four concentrations tested to a one-site dose–response equation using XLFit (IDBS) with the bottom and top parameters of the curve fixed to 0% and 100%, respectively, and the slope value fixed to 1. Secondary validations of top drug targets can be found in Supplementary Table S5.

IC_{50} Analysis

Cells were plated at a density of 1×10^4 cells/well in a 96-well plate in full media. The following day, vehicle or drug was added at 2× desired concentration to six replicate wells. Etoposide (1 mmol/L; SelleckChem) was used as a positive control for death. Cells were incubated at 37°C for 72 hours and assessed for viability by 10% Alamar Blue (Thermo). Plates were read at (F): 530/25, 590/35 in a microplate reader, and percent viability was calculated as done previously (62). IC_{50} was determined using a linear regression model (Prism 9).

NET Formation and Staining

NETs were generated and measured as previously described (81, 82). Briefly, mouse neutrophils were isolated from the bone marrow of mice using a magnetic cell separation technique with Ly6G microbeads and positive selection using LS columns (Miltenyi Biotech). The isolated neutrophils were placed in 24-well, flat-bottom plates at a density of 250,000 cells/mL in NET media (PhenolRed-free RPMI 1640 + 2% FBS) and cultured overnight with 200 nmol/L PMA (Sigma-Aldrich). Then, the medium in the well was removed, and the wells were fixed with 4% paraformaldehyde (Electron Microscopy

Sciences), followed by staining with SYTOX Green Nucleic Acid Stain (Thermo Fisher Scientific) at a final concentration of 250 nmol/L. A Nikon Eclipse TiE inverted microscope equipped with a motorized XY stage was used to image NETs. Twenty-five images were acquired per well, selected from random locations. The z-stacks per location were then combined into an extended depth-focused image. The total NET area was calculated by segmenting each image using a defined threshold pixel intensity setting. The spot detection tool in NIS-Elements Ar was used to count the number of cells per field. The sum of the total NET area in the 25 random fields of view was divided by the total number of cells in the 25 fields of view to obtain the NET area (μm)/cell.

Identification of Gene Signature Associated with PADI4; Association of Y107H with Cancer

TCGA RNA-sequencing RSEM-normalized counts were downloaded from the Xena browser (https://xenabrowser.net; ref. 83). The Liu (84) and Hugo (85) datasets were downloaded from cBioPortal (86). We selected genes with impaired transactivation in Y107H, cells whose expression levels are highly correlated with PADI4 levels across TCGA cancer types. For every cancer type, we created 100 bootstrap sample sets (using 60% of the samples in each set) to correlate PADI4 expression with that of genes with impaired transactivation in Y107H, using Spearman rank correlation. We selected four genes with the highest average correlation coefficient across different cancer types, *CEACAM21*, *IL16*, *S1PR4*, and *IL21R*. We defined a five-gene score by the average expression level (z-score transformed) of PADI4 and the four correlates of PADI4 impaired by Y107H. The five-gene score was correlated with survival across TCGA cancer types and in the Liu and Hugo melanoma anti–PD-1 datasets through log-rank through the Python lifelines package (v0.26.4; ref. 87), defining the median level of the five-gene score as a threshold. CIBERSORT (88) software was applied to TCGA samples using the default set of 22 immune cell signatures, and abundances of inferred immune cell types were correlated with the five-gene score.

For evaluating the association between African Americans, the Y107H variant, and cancer risk, we first evaluated the association between African Americans and the Y107H germline variant. Out of 9,080 TCGA patients with clinical information, four are heterozygous for the Y107H variant, of which three are African Americans. Eight hundred and two are African Americans in the complete population. Therefore, there is an enrichment of Y107H in African-descent populations with $P = 0.0026$. We then evaluated the association between Y107H and cancer within African American patients. Considering 42,038 (likely healthy) African Americans in gnomAD and 802 African Americans in TCGA (cancer positive), and that three of the total 802 African Americans with cancer are positive for the Y107H variant, whereas 37 of the total 42,038 likely healthy African Americans are positive for the Y107H variant, the association of Y107H with cancer is $P = 0.0387$.

Statistical Analysis of Data

Statistical specifications of each experiment, such as number of animals, number of tumors, biological replicates, technical replicates, precision measures (mean and ± SD), and the statistical tests used, are provided in the figures and figure legends. Unpaired two-tailed Student *t* test was used to calculate the *P* values for two-group comparisons of tumor volume changes from baseline at the end of follow-up, relative mRNA expression levels, ChIP-qPCR, colony suppression, or quantitative evaluation of IHC staining. Kaplan–Meier survival analysis was performed using the software GraphPad Prism 9 with the log-rank (Mantel–Cox) test. Densitometric measurements for quantification of immunoblot bands were done with the gel analysis software ImageJ and normalized to loading controls. Mouse experiments were not performed in a blinded manner. The following designations for levels of significance are used within this article: *, $P < 0.05$; **, $P < 0.01$; ***, $P < 0.001$; **** $P < 0.0001$; ns, not significant.

Data and Code Availability

RNA-seq data from this study are available at the Gene Expression Omnibus under accession number GSE209837. Script and instructions for code can be found at https://github.com/AuslanderLab/TP53_PADI4. Any additional information required to reanalyze the data reported in this article is available from the corresponding author upon request.

A list of key reagents is included in Supplementary Table S6.

Authors' Disclosures

A. Indeglia reports grants from the University of Pennsylvania during the conduct of the study. Y. Nefedova reports grants from the NIH/NCI during the conduct of the study, as well as grants from Jubilant Therapeutics, Active Biotech, and Buzzard Pharmaceutical outside the submitted work. J. Karanicolas reports grants from the NIH and the Pennsylvania Department of Health during the conduct of the study, as well as grants and personal fees from Triana Biomedicines outside the submitted work. No disclosures were reported by the other authors.

Authors' Contributions

A. Indeglia: Conceptualization, formal analysis, funding acquisition, investigation, writing–original draft, writing–review and editing. **J.C. Leung:** Conceptualization, investigation, methodology. **S.A. Miller:** Conceptualization, investigation, methodology, writing–review and editing. **J. Leu:** Conceptualization, formal analysis, investigation, methodology, writing–review and editing. **J.F. Dougherty:** Investigation. **N.L. Clarke:** Investigation. **N.A. Kirven:** Investigation. **C. Shao:** Conceptualization, investigation. **L. Ke:** Investigation. **S. Lovell:** Funding acquisition, investigation. **T. Barnoud:** Conceptualization, funding acquisition, investigation. **D.Y. Lu:** Investigation. **C. Lin:** Investigation. **T. Kannan:** Formal analysis. **K.P. Battaile:** Supervision, funding acquisition, investigation. **T.H.L Yang:** Formal analysis, investigation. **I. Batista Oliva:** Investigation. **D.T. Claiborne:** Conceptualization, resources, investigation. **P. Vogel:** Investigation. **L. Liu:** Investigation. **Q. Liu:** Formal analysis. **Y. Nefedova:** Funding acquisition, investigation. **J. Cassel:** Validation, investigation. **N. Auslander:** Funding acquisition, investigation, methodology, writing–review and editing. **A.V. Kossenkov:** Investigation, methodology, writing–review and editing. **J. Karanicolas:** Supervision, funding acquisition, investigation, writing–review and editing. **M.E. Murphy:** Conceptualization, resources, formal analysis, supervision, funding acquisition, writing–original draft, project administration, writing–review and editing.

Acknowledgments

We thank the Histotechnology Facility, Animal Facility, Imaging Facility, and Genomics Facility at The Wistar Institute. We acknowledge the Molecular Pathology and Imaging Core at the University of Pennsylvania, funded by the Center Molecular Studies in Digestive and Liver Diseases (NIH-P30-DK050306). We thank Xiang Hua of Fox Chase Cancer Center for CRISPR-mediated creation of Y107H and Y104H mice. We thank Xiaoxia Cui and the Genome Engineering and iPSC Center at Washington University in St. Louis for gRNA validation and cell line engineering services. We thank Phillip Wulfridge for assistance with bioinformatic analysis and Reyes Acosta and Francesco Pennino from the Claiborne lab for help with processing tissues from mice. M.E. Murphy extends gratitude to RJM. Graphic design was created using BioRender.com, for which the authors possess a license. Use of the NYX beamline 19-ID at the National Synchrotron Light Source II was supported by the New York Structural

Biology Center. NYX detector instrumentation was supported by grant S10OD030394. This research used resources of the National Synchrotron Light Source II, a U.S. Department of Energy Office of Science User Facility operated for the Department of Energy Office of Science by Brookhaven National Laboratory under contract no. DE-SC0012704. This work was supported by NIH grants CA102184 [principal investigator (PI) M.E. Murphy], CA238611 (PI M.E. Murphy), R00 CA241367 (PI T. Barnoud), and P30CA006927 (PI J. Karanicolas). A. Indeglia was supported in part by T32 GM008216, J.C. Leung was supported in part by T32 CA009171-43 and the Wistar Accelerator Postdoctoral Award, and S.A. Miller was supported in part by T32 CA009035.

The publication costs of this article were defrayed in part by the payment of publication fees. Therefore, and solely to indicate this fact, this article is hereby marked "advertisement" in accordance with 18 USC section 1734.

Note

Supplementary data for this article are available at Cancer Discovery Online (http://cancerdiscovery.aacrjournals.org/).

Received November 22, 2022; revised March 21, 2023; accepted April 6, 2023; published first May 4, 2023.

REFERENCES

1. Fischer M. Census and evaluation of p53 target genes. Oncogene 2017;36:3943–56.
2. Pfister NT, Prives C. Transcriptional regulation by wild-type and cancer-related mutant forms of p53. Cold Spring Harb Perspect Med 2017;7:a026054.
3. Vousden KH, Prives C. Blinded by the light: the growing complexity of p53. Cell 2009;137:413–31.
4. Kandoth C, McLellan MD, Vandin F, Ye K, Niu B, Lu C, et al. Mutational landscape and significance across 12 major cancer types. Nature 2013;502:333–9.
5. Zhang C, Liu J, Xu D, Zhang T, Hu W, Feng Z. Gain-of-function mutant p53 in cancer progression and therapy. J Mol Cell Biol 2020;12:674–87.
6. Kennedy MC, Lowe SW. Mutant p53: it's not all one and the same. Cell Death Differ 2022;29:983–7.
7. Oren M, Rotter V. Mutant p53 gain-of-function in cancer. Cold Spring Harb Perspect Biol 2010;2:a001107.
8. Thomas AF, Kelly GL, Strasser A. Of the many cellular responses activated by TP53, which ones are critical for tumour suppression? Cell Death Differ 2022;29:961–71.
9. Jennis M, Kung CP, Basu S, Budina-Kolomets A, Leu JI, Khaku S, et al. An African-specific polymorphism in the TP53 gene impairs p53 tumor suppressor function in a mouse model. Genes Dev 2016;30:918–30.
10. Powers J, Pinto EM, Barnoud T, Leung JC, Martynyuk T, Kossenkov AV, et al. A rare TP53 mutation predominant in Ashkenazi Jews confers risk of multiple cancers. Cancer Res 2020;80:3732–44.
11. Olivier M, Hollstein M, Hainaut P. TP53 mutations in human cancers: origins, consequences, and clinical use. Cold Spring Harb Perspect Biol 2010;2:a001008–a.
12. Murphy ME, Liu S, Yao S, Huo D, Liu Q, Dolfi SC, et al. A functionally significant SNP in TP53 and breast cancer risk in African-American women. NPJ Breast Cancer 2017;3:1–5.
13. Nakano K, Vousden KH. PUMA, a novel proapoptotic gene, is induced by p53. Mol Cell 2001;7:683–94.
14. Shibue T, Takeda K, Oda E, Tanaka H, Murasawa H, Takaoka A, et al. Integral role of Noxa in p53-mediated apoptotic response. Genes Dev 2003;17:2233–8.
15. el-Deiry WS, Tokino T, Velculescu VE, Levy DB, Parsons R, Trent JM, et al. WAF1, a potential mediator of p53 tumor suppression. Cell 1993;75:817–25.
16. Valente LJ, Gray DH, Michalak EM, Pinon-Hofbauer J, Egle A, Scott CL, et al. p53 efficiently suppresses tumor development in the complete absence of its cell-cycle inhibitory and proapoptotic effectors p21, Puma, and Noxa. Cell Rep 2013;3:1339–45.
17. Brugarolas J, Chandrasekaran C, Gordon JI, Beach D, Jacks T, Hannon GJ. Radiation-induced cell cycle arrest compromised by p21 deficiency. Nature 1995;377:552–7.
18. Villunger A, Michalak EM, Coultas L, Müllauer F, Böck G, Ausserlechner MJ, et al. p53- and drug-induced apoptotic responses mediated by BH3-only proteins puma and noxa. Science 2003;302:1036–8.
19. Bieging-Rolett KT, Kaiser AM, Morgens DW, Boutelle AM, Seoane JA, Van Nostrand EL, et al. Zmat3 is a key splicing regulator in the p53 tumor suppression program. Mol Cell 2020;80:452–69.
20. Tanikawa C, Espinosa M, Suzuki A, Masuda K, Yamamoto K, Tsuchiya E, et al. Regulation of histone modification and chromatin structure by the p53–PADI4 pathway. Nat Commun 2012;3:676.
21. Wang Y, Allis CD. Human PAD4 regulates histone arginine methylation levels via demethylimination. Science 2004;306:279–83.
22. Doffe F, Carbonnier V, Tissier M, Leroy B, Martins I, Mattsson JSM, et al. Identification and functional characterization of new missense SNPs in the coding region of the TP53 gene. Cell Death Differ 2021;28:1477–92.
23. Kato S, Han SY, Liu W, Otsuka K, Shibata H, Kanamaru R, et al. Understanding the function–structure and function–mutation relationships of p53 tumor suppressor protein by high-resolution missense mutation analysis. Proc Natl Acad Sci U S A 2003;100:8424–9.
24. Klimovich B, Merle N, Neumann M, Elmshäuser S, Nist A, Mernberger M, et al. p53 partial loss-of-function mutations sensitize to chemotherapy. Oncogene 2022;41:1011–23.
25. Reinbold M, Luo JL, Nedelko T, Jerchow B, Murphy ME, Whibley C, et al. Common tumour p53 mutations in immortalized cells from Hupki mice heterozygous at codon 72. Oncogene 2008;27:2788–94.
26. Frank AK, Leu JIJ, Zhou Y, Devarajan K, Nedelko T, Klein-Szanto A, et al. The codon 72 Polymorphism of p53 regulates interaction with NF-κB and transactivation of genes involved in immunity and inflammation. Mol Cell Biol 2011;31:1201–13.
27. Minter LM, Dickinson ES, Naber SP, Jerry DJ. Epithelial cell cycling predicts p53 responsiveness to γ-irradiation during post-natal mammary gland development. Development 2002;129:2997–3008.
28. MacCallum DE, Hupp TR, Midgley CA, Stuart D, Campbell SJ, Harper A, et al. The p53 response to ionising radiation in adult and developing murine tissues. Oncogene 1996;13:2575–87.
29. Rohrbach AS, Slade DJ, Thompson PR, Mowen KA. Activation of PAD4 in NET formation. Front Immunol 2012;3:1–10.
30. Weinberg RL, Veprintsev DB, Bycroft M, Fersht AR. Comparative binding of p53 to its promoter and DNA recognition elements. J Mol Biol 2005;348:589–96.
31. Muller PA, Vousden KH. Mutant p53 in cancer: new functions and therapeutic opportunities. Cancer Cell 2014;25:304–17.
32. Muller PA, Vousden KH. p53 mutations in cancer. Nat Cell Biol 2013;15:2–8.
33. Barnoud T, Budina-Kolomets A, Basu S, Leu JI, Good M, Kung CP, et al. Tailoring chemotherapy for the African-centric S47 variant of TP53. Cancer Res 2018;78:5694–705.
34. Lampa M, Arlt H, He T, Ospina B, Reeves J, Zhang B, et al. Glutaminase is essential for the growth of triple-negative breast cancer cells with a deregulated glutamine metabolism pathway and its suppression synergizes with mTOR inhibition. PLoS One 2017;12:e0185092.
35. Leung JC, Leu JIJ, Indeglia A, Kannan T, Clarke NL, Kirven NA, et al. Common activities and predictive gene signature identified for genetic hypomorphs of TP53. Proc Natl Acad Sci U S A 2023;120:e2212940120.
36. Tanikawa C, Ueda K, Nakagawa H, Yoshida N, Nakamura Y, Matsuda K. Regulation of protein citrullination through p53/PADI4 network in DNA damage response. Cancer Res 2009;69:8761–9.

37. Chang X, Han J, Pang L, Zhao Y, Yang Y, Shen Z. Increased PADI4 expression in blood and tissues of patients with malignant tumors. BMC Cancer 2009;9:40.
38. Li P, Yao H, Zhang Z, Li M, Luo Y, Thompson PR, et al. Regulation of p53 target gene expression by peptidylarginine deiminase 4. Mol Cell Biol 2008;28:4745–58.
39. Mirabello L, Yeager M, Mai PL, Gastier-Foster JM, Gorlick R, Khanna C, et al. Germline TP53 variants and susceptibility to osteosarcoma. J Natl Cancer Inst 2015;107:djv101.
40. Gnanapradeepan K, Indeglia A, Stieg DC, Clarke N, Shao C, Dougherty JF, et al. PLTP is a p53 target gene with roles in cancer growth suppression and ferroptosis. J Biol Chem 2022;298:102637.
41. Liu GY, Liao YF, Chang WH, Liu CC, Hsieh MC, Hsu PC, et al. Overexpression of peptidylarginine deiminase IV features in apoptosis of haematopoietic cells. Apoptosis 2006;11:183–96.
42. Chang X, Fang K. PADI4 and tumourigenesis. Cancer Cell Int 2010;10:7.
43. Cui YY, Yan L, Zhou J, Zhao S, Zheng YB, Sun BH, et al. The role of peptidylarginine deiminase 4 in ovarian cancer cell tumorigenesis and invasion. Tumour Biol 2016;37:5375–83.
44. Gijon M, Metheringham RL, Toss MS, Paston SJ, Durrant LG. The clinical and prognostic significance of protein arginine deiminases 2 and 4 in colorectal cancer. Pathobiology 2022;89:38–48.
45. Christophorou MA, Castelo-Branco G, Halley-Stott RP, Oliveira CS, Loos R, Radzisheuskaya A, et al. Citrullination regulates pluripotency and histone H1 binding to chromatin. Nature 2014;507:104–8.
46. Slade DJ, Horibata S, Coonrod SA, Thompson PR. A novel role for protein arginine deiminase 4 in pluripotency: the emerging role of citrullinated histone H1 in cellular programming. Bioessays 2014;36:736–40.
47. Wang Y, Lyu Y, Tu K, Xu Q, Yang Y, Salman S, et al. Histone citrullination by PADI4 is required for HIF-dependent transcriptional responses to hypoxia and tumor vascularization. Sci Adv 2021;7:eabe3771.
48. Moshkovich N, Ochoa HJ, Tang B, Yang HH, Yang Y, Huang J, et al. Peptidylarginine deiminase IV (PADI4) regulates breast cancer stem cells via a novel tumor cell-autonomous suppressor role. Cancer Res 2020;80:2125–37.
49. Stadler SC, Vincent CT, Fedorov VD, Patsialou A, Cherrington BD, Wakshlag JJ, et al. Dysregulation of PAD4-mediated citrullination of nuclear GSK3 activates TGF-signaling and induces epithelial-to-mesenchymal transition in breast cancer cells. Proc Natl Acad Sci U S A 2013;110:11851–6.
50. Zhou Q, Song C, Liu X, Qin H, Miao L, Zhang X. Peptidylarginine deiminase 4 overexpression resensitizes MCF-7/ADR breast cancer cells to adriamycin via GSK3β/p53 activation. Cancer Manag Res 2019;11:625–36.
51. Yao H, Li P, Venters BJ, Zheng S, Thompson PR, Pugh BF, et al. Histone Arg modifications and p53 regulate the expression of OKL38, a mediator of apoptosis. J Biol Chem 2008;283:20060–8.
52. Guo Q, Fast W. Citrullination of inhibitor of growth 4 (ING4) by peptidylarginine deminase 4 (PAD4) disrupts the interaction between ING4 and p53. J Biol Chem 2011;286:17069–78.
53. Li P, Wang D, Yao H, Doret P, Hao G, Shen Q, et al. Coordination of PAD4 and HDAC2 in the regulation of p53-target gene expression. Oncogene 2010;29:3153–62.
54. Fan L, Zong M, Gong R, He D, Li N, Sun LS, et al. PADI4 epigenetically suppresses p21 transcription and inhibits cell apoptosis in Fibroblast-like synoviocytes from rheumatoid arthritis patients. Int J Biol Sci 2017;13:358–66.
55. Adrover JM, McDowell SAC, He XY, Quail DF, Egeblad M. NETworking with cancer: the bidirectional interplay between cancer and neutrophil extracellular traps. Cancer Cell 2023;41:505–26.
56. Suzuki A, Yamada R, Chang X, Tokuhiro S, Sawada T, Suzuki M, et al. Functional haplotypes of PADI4, encoding citrullinating enzyme peptidylarginine deiminase 4, are associated with rheumatoid arthritis. Nat Genet 2003;34:395–402.
57. Zheng Y, Zhao G, Xu B, Liu C, Li C, Zhang X, et al. PADI4 has genetic susceptibility to gastric carcinoma and upregulates CXCR2, KRT14 and TNF-α expression levels. Oncotarget 2016;7:62159–76.
58. Basu S, Barnoud T, Kung C-P, Reiss M, Murphy ME. The African-specific S47 polymorphism of p53 alters chemosensitivity. Cell Cycle 2016;15:2557–60.
59. Barnoud T, Parris JLD, Murphy ME. Tumor cells containing the African-centric S47 variant of TP53 show increased Warburg metabolism. Oncotarget 2019;10:1217–23.
60. Tajan M, Hock AK, Blagih J, Robertson NA, Labuschagne CF, Kruiswijk F, et al. A role for p53 in the adaptation to glutamine starvation through the expression of SLC1A3. Cell Metab 2018;28:721–36.
61. Lowman XH, Hanse EA, Yang Y, Ishak Gabra MB, Tran TQ, Li H, et al. p53 promotes cancer cell adaptation to glutamine deprivation by upregulating Slc7a3 to increase arginine uptake. Cell Rep 2019;26:3051–60.
62. Parris JLD, Barnoud T, Leu JI, Leung JC, Ma W, Kirven NA, et al. HSP70 inhibition blocks adaptive resistance and synergizes with MEK inhibition for the treatment of NRAS-mutant melanoma. Cancer Res Commun 2021;1:17–29.
63. Webster MR, Fane ME, Alicea GM, Basu S, Kossenkov AV, Marino GE, et al. Paradoxical role for wild-type p53 in driving therapy resistance in melanoma. Mol Cell 2020;77:633–44.
64. Serrano M, Lin AW, McCurrach ME, Beach D, Lowe SW. Oncogenic ras provokes premature cell senescence associated with accumulation of p53 and p16INK4a. Cell 1997;88:593–602.
65. Langmead B, Salzberg SL. Fast gapped-read alignment with Bowtie 2. Nat Methods 2012;9:357–9.
66. Li B, Dewey CN. RSEM: accurate transcript quantification from RNA-seq data with or without a reference genome. BMC Bioinf 2011;12:323.
67. Love MI, Huber W, Anders S. Moderated estimation of fold change and dispersion for RNA-seq data with DESeq2. Genome Biol 2014;15:550.
68. Xie Z, Bailey A, Kuleshov MV, Clarke DJB, Evangelista JE, Jenkins SL, et al. Gene set knowledge discovery with enrichr. Curr Protoc. 2021;1:e90.
69. Kabsch W. Automatic indexing of rotation diffraction patterns. J Appl Crystallogr 1988;21:67–72.
70. Kabsch W. XDS. Acta Crystallogr D Biol Crystallogr 2010;66(Pt 2):125–32.
71. Vonrhein C, Flensburg C, Keller P, Sharff A, Smart O, Paciorek W, et al. Data processing and analysis with the autoPROC toolbox. Acta Crystallogr D Biol Crystallogr 2011;67(Pt 4):293–302.
72. Evans PR. An introduction to data reduction: space-group determination, scaling and intensity statistics. Acta Crystallogr D Biol Crystallogr 2011;67(Pt 4):282–92.
73. McCoy AJ, Grosse-Kunstleve RW, Adams PD, Winn MD, Storoni LC, Read RJ. Phaser crystallographic software. J Appl Cryst 2007;40:658–74.
74. Adams PD, Afonine PV, Bunkóczi G, Chen VB, Davis IW, Echols N, et al. PHENIX: a comprehensive Python-based system for macromolecular structure solution. Acta Crystallogr D Biol Crystallogr 2010;66(Pt 2):213–21.
75. Emsley P, Lohkamp B, Scott WG, Cowtan K. Features and development of Coot. Acta Crystallogr D Biol Crystallogr 2010;66(Pt 4):486–501.
76. Chen VB, Arendall WB 3rd, Headd JJ, Keedy DA, Immormino RM, Kapral GJ, et al. MolProbity: all-atom structure validation for macromolecular crystallography. Acta Crystallogr D Biol Crystallogr 2010;66(Pt 1):12–21.
77. Potterton L, McNicholas S, Krissinel E, Gruber J, Cowtan K, Emsley P, et al. Developments in the CCP4 molecular-graphics project. Acta Crystallogr D Biol Crystallogr 2004;60(Pt 12 Pt 1):2288–94.
78. Krissinel E. Enhanced fold recognition using efficient short fragment clustering. J Mol Biochem 2012;1:76–85.
79. Winn MD, Ballard CC, Cowtan KD, Dodson EJ, Emsley P, Evans PR, et al. Overview of the CCP4 suite and current developments. Acta Crystallogr D Biol Crystallogr 2011;67(Pt 4):235–42.
80. Leone RD, Zhao L, Englert JM, Sun I-M, Oh M-H, Sun I-H, et al. Glutamine blockade induces divergent metabolic programs to overcome tumor immune evasion. Science 2019;366:1013–21.
81. Li M, Lin C, Deng H, Strnad J, Bernabei L, Vogl DT, et al. A novel peptidylarginine deiminase 4 (PAD4) inhibitor BMS-P5 blocks formation

of neutrophil extracellular traps and delays progression of multiple myeloma. Mol Cancer Ther 2020;19:1530–8.
82. Li M, Lin C, Leso A, Nefedova Y. Quantification of citrullinated histone H3 bound DNA for detection of neutrophil extracellular traps. Cancers (Basel) 2020;12:3424.
83. Goldman MJ, Craft B, Hastie M, Repečka K, McDade F, Kamath A, et al. Visualizing and interpreting cancer genomics data via the Xena platform. Nat Biotechnol 2020;38:675–8.
84. Liu D, Schilling B, Liu D, Sucker A, Livingstone E, Jerby-Arnon L, et al. Integrative molecular and clinical modeling of clinical outcomes to PD1 blockade in patients with metastatic melanoma. Nat Med 2019;25:1916–27.
85. Hugo W, Zaretsky JM, Sun L, Song C, Moreno BH, Hu-Lieskovan S, et al. Genomic and transcriptomic features of response to anti–PD-1 therapy in metastatic melanoma. Cell 2016;165:35–44.
86. Gao J, Aksoy BA, Dogrusoz U, Dresdner G, Gross B, Sumer SO, et al. Integrative analysis of complex cancer genomics and clinical profiles using the cBioPortal. Sci Signal 2013;6:pl1.
87. Davidson-Pilon C. Lifelines: survival analysis in Python. J Open Source Software 2019;4:1317.
88. Newman AM, Liu CL, Green MR, Gentles AJ, Feng W, Xu Y, et al. Robust enumeration of cell subsets from tissue expression profiles. Nat Methods 2015;12:453–7.